



GROUP NO. 20
AVAILABILITY Open

**Department of Civil Engineering and Energy Technology**  
Mailing address: PB 4. St. Olavs plass, 0130 Oslo  
Streetaddress: Pilestredet 35, Oslo

Phone: 67 23 50 00  
www.hioa.no

## BACHELOR'S THESIS

TITLE Pipe losses: A numerical study using Computational Fluid Dynamics	DATE 22.05.2018
	NUMBER OF PAGES/ATTACHEMENTS 43/7
AUTHORS Eskil Bro Ørvik Kjell Løvtangen Borgen	SUPERVISER Arnab Chaudhuri
DONE IN COLLABORATION WITH Oslo Metropolitan University	CONTACT Arnab Chaudhuri

ABSTRACT This report contains the results from the simulations done in STAR-CCM+ to predict pipe losses, including a validation case with straight smooth/rough pipes, and smooth pipes with 90 degree bends. Results show excellent validation of predicting the major loss coefficient of smooth/rough pipes with a percentage of error below 0.7. The results are compared with previous research papers and ultimately led to an equation, making the Reynolds number a parameter when calculating the minor loss coefficient for pipe bends.
--

3 keywords:
Wall roughness
Minor loss coefficient
CFD

## Project Description

In order to obtain a fully functional, energy effective ventilation system, several factors must be optimized, ranging from the volume of air needed to the pump requirements. The importance of a satisfactory indoor climate is a continuous science relevant to research regarding among others efficiency and health in the workplace. Currently, the balanced ventilation system is a required minimum for most buildings, meaning that the same amount of air being distributed must be exhausted. This and other requirements like the energy efficiency claim contribute to the need of systems capable of delivering set requirements at an affordable consumer price.

Calculating the major and minor losses in a ventilation system are important regarding dimensioning of the ventilation unit. Here, the energy usage can be optimized if the calculations are correct.

Major losses are due to friction in a straight pipe or duct section, variable by the roughness of the wall and the velocity of the fluid flow. Depending on the material used for the pipes or ducts, these vary also with time on account of e.g. corrosion. Minor losses are due to components in the system like bends, valves and various junctions.

Due to insufficient laboratory data, minor loss coefficients are often referred to in textbooks as constant zeta values, independent of Reynolds number and diameter. There is therefore now interest for using computational fluid dynamics to fill the gaps, ultimately leading to making the Reynolds number a parameter when calculating minor loss coefficients.

Tasks for this work are:

- To make a detailed validation of the CFD models regarding turbulent flow in straight smooth/rough pipes with a circular cross section and comparing them to classical formulas like the Colebrook and Haaland equations.
- To simulate flow through a  $90^\circ$  bend in smooth pipe to obtain zeta values which are to be compared to previous research.

## Acknowledgements

We would like to express our deepest and most sincere gratitude to our supervisor Arnab Caudhuri, associate Professor at OsloMet, for guidance, suggestions, encouragement and support throughout this work.

In the last few months, from barely hearing about the term CFD, our learning curve has been steep. While finding a general interest in contributing to pressure loss calculations, we came upon a thesis with a relevant objective, proposed by Peter Schild, Professor at OsloMet. He shed light on the missing data regarding the minor loss coefficients in ducts, mainly that current values are excluding the Reynolds number. Apparently the Reynolds number is often excluded when calculating the so-called zeta values, meaning there is presently an interest in using CFD to fill the gaps and ultimately being able to resolve minor pressure loss with the Reynolds number as a parameter. We would like to thank Peter for introducing this topic to us.

We would also like to thank Ole Melhus, associate Professor at OsloMet for the guidance received when initially taking on the complex CFD tool that is STAR-CCM+. Simultaneously we would like to thank the Campus of OsloMet for providing the technical equipment required to do this work.

Last, but not least, we would like to thank our family, friends and fellow students for moral support, comforting words when things seemed impossible and for cheering us on when our work came close to finished.

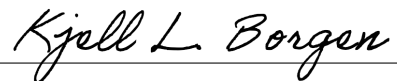
Thank you all.

Eskil Bro Ørvik & Kjell Løvtangen Borgen



---

Eskil Bro Ørvik



---

Kjell Løvtangen Borgen

Date: 22.05.18

Place: Oslo

## Abstract

The objective of this work is to ultimately shed light on the effects of both Reynolds number and diameter in ventilation pipes on pressure loss. Numerical simulations are performed using STAR-CCM+, a commercial CFD software. Classical formulas like the Colebrook and Haaland equations (the Moody chart), have been the basis for the validation of the chosen numerical models. Friction factors for smooth and rough pipes with three different roughness parameters are simulated. By comparing the simulated results with the classical formulas, we have been able to determine the accuracy of the method. An extensive analysis with varying  $y^+$  has been presented to achieve the high accuracy of the CFD prediction. This has been obtained by realizable  $\kappa - \epsilon$  turbulence model with  $1 < y^+ < 14$ . Results show excellent validation of predicting the major loss coefficient of smooth/rough pipes with a percentage of error below 0.7.

A detailed parametric study is performed to elucidate how the minor loss coefficient depends on the Reynolds number and the diameter for  $90^\circ$  smooth pipe bends. In these cases, the Reynolds stress model (RSM) as turbulence model performed better. We found that the minor loss coefficient is predominantly a function of Reynolds number, and it does not vary appreciably with diameters for a fixed Reynolds number. A curve fitting shows the functional dependency as  $C_{Re} = 21.6(Re)^{-0.254}$  for  $90^\circ$  bend in the range of  $10,000 \leq Re \leq 500,000$ .

# Contents

<b>1</b>	<b>Introduction</b>	<b>6</b>
<b>2</b>	<b>Objective</b>	<b>8</b>
<b>3</b>	<b>Theory</b>	<b>9</b>
3.1	Background . . . . .	9
3.2	Turbulent Flow in Pipes . . . . .	11
3.2.1	Turbulent Velocity Profile . . . . .	12
3.2.2	Major Losses . . . . .	14
3.2.3	Minor Losses . . . . .	15
3.2.4	Mach number . . . . .	16
3.3	Governing Equations for Fluid Flow . . . . .	16
3.3.1	RANS . . . . .	17
3.4	CFD Technique & STAR-CCM+ . . . . .	19
3.4.1	Pre-processor . . . . .	19
3.4.2	Solver . . . . .	19
3.4.3	Post-processor . . . . .	19
<b>4</b>	<b>Method</b>	<b>20</b>
4.1	Geometry . . . . .	20
4.2	Mesh . . . . .	21
4.3	Boundaries . . . . .	21
4.4	Wall Treatment . . . . .	21
4.5	Roughness Modeling . . . . .	22
<b>5</b>	<b>Problem Setup</b>	<b>24</b>
5.1	Straight Pipe . . . . .	24
5.2	90 Degree Bend . . . . .	28
5.3	Matlab . . . . .	32
<b>6</b>	<b>Results and Discussion</b>	<b>33</b>
6.1	Straight Pipe . . . . .	33
6.2	90 Degree Bend . . . . .	36
6.2.1	Varying Diameter . . . . .	38
6.2.2	Varying Reynolds Number . . . . .	39
<b>7</b>	<b>Conclusions</b>	<b>42</b>
	<b>References</b>	<b>43</b>
<b>8</b>	<b>Appendix A. Residuals Straight Pipe</b>	<b>44</b>
<b>9</b>	<b>Appendix B. Residuals 90 Degree Bend</b>	<b>50</b>

# 1 Introduction

*“A well functioning ventilation system is not to be heard, not to be seen, shall not gather dust, shall not distribute pollutions or smells, shall not distribute drafts and shall be energy effective. It should only distribute comfort” [1].*

The ventilation system is considered to be a relatively fresh business, however processing of air has been preformed for many years, all the way back to the ancient Rome. The mining business were the first to make use of fans to distribute sufficient air flow in the mines in the early 1800's. The concentration of  $CO_2$  were determined by Max von Pettenkofer in 1858 to be less than 1000 ppm (parts per million) in schools, which still is a reference value used today.

In order to maintain satisfactory indoor air quality, an effective ventilation system is required. The system has to be tailored based on the needs of set building or apartment. This includes not only sufficient amount of air distributed, but also the quality of the air itself according to current claims. The air outside is often polluted with a number of health threatening particles like dust or industrial exhaust, meaning the ventilation unit is in need of a filtering system.

The ventilation system as we know it today, balanced ventilation, were common in residential housing by the 2000's. This was a result of the energy efficiency claim that required heat recovery. A balanced system means that the amount of air distributed to the building or room must be equal to the amount of air exhausted. Simultaneously there are claims regarding heat recovery in the unit to guarantee energy efficiency. General claims regarding indoor air quality have been continuously revised, providing the utmost quality and efficiency delivered by the ventilation systems, and they still are.

In addition to the regular ducts and pipes, there are several components contributing to a balanced ventilation system, including dampers, fans and filters to name a few, all of which obviously have great impact on the characteristics of the fluid flow from the air intake to the air exhaust. One might think that these components are the main reasons for e.g. pressure loss. However, the ducts themselves have a huge impact as well regarding wall roughness and when facing bends or T-junctions. Figure 1 is an illustration of an industrial ventilation system with bends and components typically occurring.



Figure 1: Visualization of ventilation system [2]

Major losses are associated with frictional energy loss per length of pipe, depending on the flow velocity, pipe length, pipe diameter and a friction factor based on the roughness of the pipe, and whether the flow is laminar or turbulent. Pressure loss due to various bends and junctions throughout the duct network are called minor losses. In order to calculate pressure loss due to these losses, experimental and empirical studies have granted constant minor loss coefficients, or zeta values.

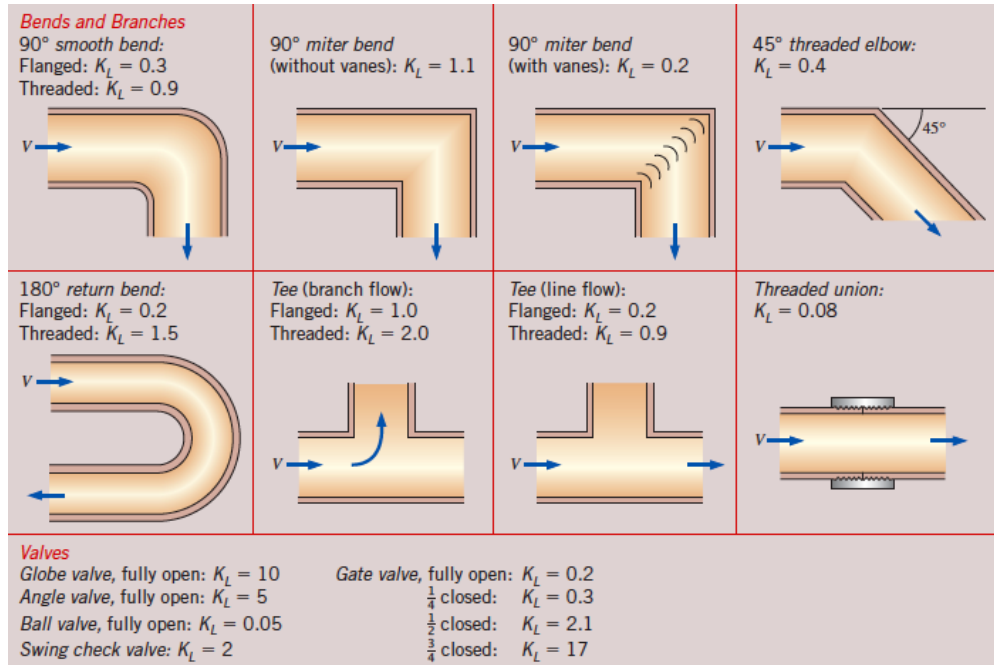


Figure 2: Zeta Values [3]

As shown in figure 2, where zeta values are referred to as  $K_L$  values, the values are completely independent of diameter and provided by the manufacturers. However, for the last 30 years we have known that traditional “minor loss coefficients” are actually highly dependent on both the diameter and the Reynolds number.

Recent studies, such as the European Report [4] ran simulations using varying Reynolds numbers, concluding they indeed have an effect on pressure loss. However in the summary of the report, all information concerning Reynolds number variation was excluded. The work in this thesis will contribute to the missing data, regardless of the results, to create awareness on the importance of Reynolds number in pressure loss. The article mentioned above discussed in total six different components, one of which are of interest in this report, a smooth 90° bend. Other research works reported by Salehi and Gutovic [5] [6] also explored the effects of Reynolds number in pressure loss. By comparing previous data, generated from different users, using different models and having various ranges in geometry, their findings include interesting predictions in which we may compare with our findings in this work.

## 2 Objective

Due to insufficient laboratory measurement data, we are not able to make correlations with Reynolds number as a parameter for minor loss coefficient. As a result of the missing data, textbooks tabulate constant zeta values as correction factors for various duct components. Even textbooks warn against using the stated zeta values, as they may differ considerably based on manufacturers data and strongly recommend using their values [3].

In order to help understand the effect of varying Reynolds number and diameter in duct components regarding pressure loss, the interest in using computational fluid dynamics (from now on referred to as CFD) is now present. By using experimental data and classical formulas like the Haaland and Colebrook equations and the Moody chart, we aim to validate our cases to insure the accuracy using a CFD software tool. Computational fluid dynamics allows us to compute complex fluid flow behavior using numerical algorithms.

The objectives for the present thesis are:

1. To make a detailed validation of the CFD models regarding turbulent and rough fluid flow by analyzing friction factor of a straight pipe with a circular cross section. We aim to keep the validation case within a range of Reynolds numbers  $5 \cdot 10^4 \leq Re \leq 5 \cdot 10^5$  and roughness  $0 \leq \epsilon/D \leq 0.0009$ .
2. When obtaining satisfactory results, we aim to simulate flow in the infamous  $90^\circ$  smooth bend, to once and for all confirm the effects of Reynolds number and diameter on pressure loss in ventilation ducts. This will lay the groundwork for the Reynolds number being implemented as a parameter for future minor loss calculations in ventilation systems.



## 3 Theory

### 3.1 Background

It's been known for more than 30 years that the Reynolds number affects the pressure loss a great deal, but for now the minor loss coefficients are determined by constant “zeta” values, and without the Reynolds number as an actual parameter. This work is ultimately meant to focus this problem. To be able to fill the current gaps regarding determining pressure loss factors correctly we have to first understand the physics behind internal fluid flow in pipes and ducts.

Liquid or gas flow through pipes or ducts is commonly used in heating and cooling applications and fluid distribution networks. In the present study, mainly, we will be dealing with the distribution of air in a ventilation system. Friction, based on major and minor losses, is used to determine the pumping power requirement and naturally we want to be able to determine which capacity our system needs with cost and energy efficiency. In order to do this properly, the pressure loss throughout the system needs to be calculated. Theoretical analysis and experimental results are often used when solving these problems, making the final results within 90% or less in accuracy. We believe that by correlating the Reynolds number as a direct parameter to the pressure loss calculations, we could help fill that current gap and contribute to more efficient systems.

Osborne Reynolds discovered laminar and turbulent flow in pipes and ducts over a century ago [3], which evidently led to Reynolds number. The number is acquired by dividing inertial forces by viscous forces,

$$Re = \frac{U_{avg}L}{\nu} = \frac{\rho U_{avg}L}{\mu} = \frac{Inertial\ forces}{Viscous\ forces} \quad (1)$$

where  $U_{avg}$  is the average flow velocity [m/s],  $L$  is the characteristic length of the geometry [m],  $\nu = \frac{\mu}{\rho}$  is the kinematic viscosity [ $m^2/s$ ] and  $\mu$  is the dynamic viscosity [kg/ms].



Figure 3: Flow regimes of a candle smoke plume [3]

We will primarily be dealing with pipe problems, which gives us a Reynolds number greater than 4000 as turbulent flow. The characteristics of turbulent flow can be shown by e.g. figure 3, where smoke is rising from a lit candle. At some point the smoke plume starts fluctuating and seems to be chaotic.

For internal flow in pipes the characteristic length  $L$  is the hydraulic diameter  $D$ . This is defined by:

$$D = \frac{4A_c}{p} \quad (2)$$

where  $A_c$  is the cross-sectional area of the pipe and  $p$  is its wetted perimeter.

Figure 4 shows the  $D$ 's for pipes and ducts with various cross sections.

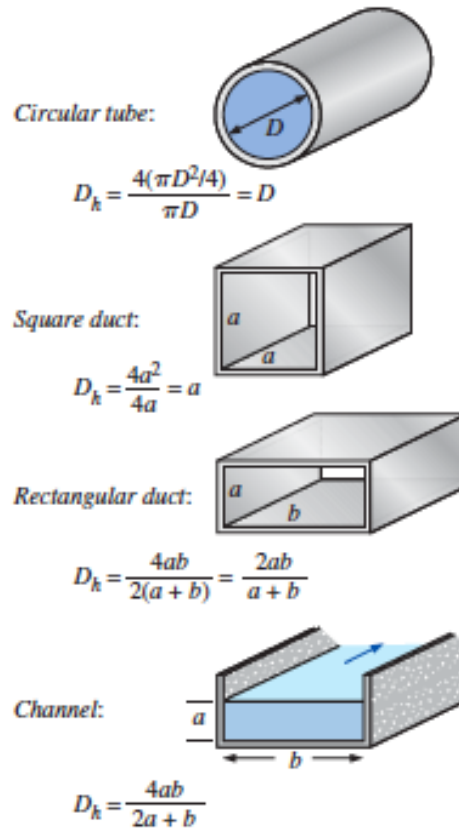


Figure 4: Hydraulic diameter for various geometries [3]

### 3.2 Turbulent Flow in Pipes

In this thesis the work will exclusively consider turbulent flow, as most flows encountered in engineering practice today are. Turbulent flow is a complex mechanism dominated by flow fluctuations and it is important to understand how this affects the wall shear stress. Our understanding of turbulent flows are far from resolved, in spite of tremendous work done in this area. One must rely on previously obtained data from experimental and empirical studies when validating any ongoing work.

For internal flow in pipes the Reynolds number must be of a certain value to be considered turbulent. Under most practical conditions. the flow in a circular pipe is laminar for  $Re \leq 2300$ , fully turbulent for  $Re \geq 4000$  and transitional in between.

Turbulent flows are defined by fluctuations, or so-called **eddies**, generating large energy, momentum, heat and mass transfer. As a result, turbulent flows are associated with much higher values of friction, heat transfer and mass transfer coefficients. The chaotic fluctuations of fluid particles play a dominating role in transport of mass, momentum and energy.

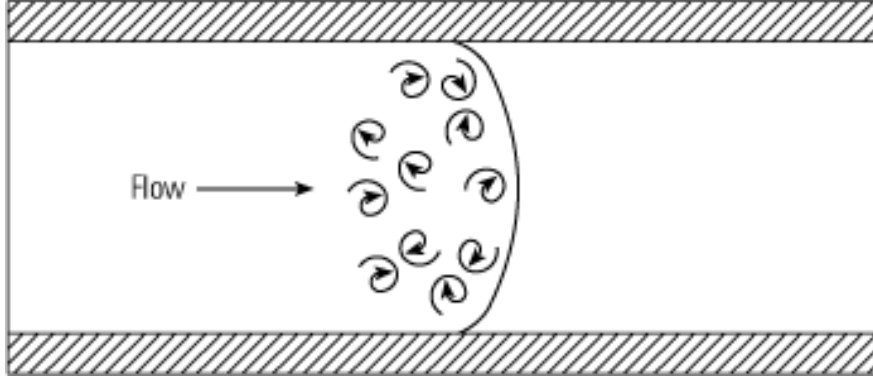


Figure 5: Eddies in Turbulent Flow [7]

The eddies (see figure 5) vary strongly in size and therefore also in energy, heat and mass transfer. The largest turbulent eddies interact with and extract energy from the mean flow by a process called **vortex stretching**. This is in CFD usage defined as a length parameter, called the turbulent length scale. The presence of mean velocity gradients in sheared flows distorts the rotational turbulent eddies. Suitably aligned eddies are stretched because one end is forced to move faster than the other [8].

### 3.2.1 Turbulent Velocity Profile

The velocity profile for laminar flow is typically parabolic when fully developed, and defined as:

$$u(r) = u_{max} \left[ 1 - \left( \frac{r}{R} \right)^2 \right] \quad (3)$$

where  $R$  is the pipe radius,  $r$  is a variable distance from the center of the pipe and  $u_{max}$  is the maximum velocity inside of the pipe. The profile is much fuller with turbulent flow, with a sharp drop near the pipe wall. Figure 6 (top) shows the parabolic profile for laminar flow.

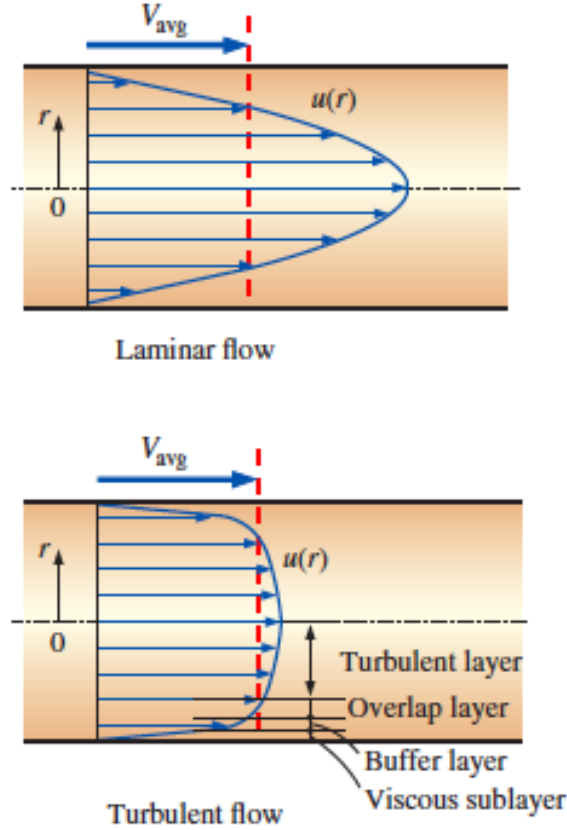


Figure 6: Velocity Profile [3]

Turbulent flow along a wall consists of four regions, characterized by the distance from the wall. The thickness of the viscous sublayer is typically much less than 1 percent of the of the pipe diameter, but this thin layer plays a dominant role on flow characteristics because of the large velocity gradients it involves. The eddy motion near the wall is dampened, and the flow in this layer is essentially laminar. The shear stress consists of laminar shear stress and is proportional to the fluid viscosity. Experiments confirm that the velocity profile in the viscous sublayer is nearly linear. The wall shear stress can then be expressed as

$$\tau_w = \mu \left( \frac{\partial u}{\partial y} \right)_{y=0} \quad (4)$$

$$\tau_w = \mu \left( \frac{u}{y} \right) = \rho \nu \left( \frac{u}{y} \right) \quad (5)$$

$$\frac{\tau_w}{\rho} = \frac{\nu u}{y}. \quad (6)$$

where  $\mu$  is the dynamic viscosity,  $u$  is the flow velocity parallel to the wall and  $y$  is the distance from the wall. The shear stress is a force whom is causing drag to the fluid flow.  $\frac{\tau_w}{\rho}$  is frequently encountered when dealing with a turbulent flow. The friction velocity  $u_\tau$  is defined as the square root of this relation so that

$u_\tau = \sqrt{\frac{\tau_w}{\rho}}$ . The velocity profile in the viscous sublayer is expressed in dimensionless form as:  $\frac{u}{u_\tau} = \frac{u_\tau y}{\nu}$ , and is known as the law of the wall.  $\frac{u_\tau y}{\nu}$  is commonly referred to as a non-dimensional distance  $y^+$ , where  $y$  is the distance to the first wall-cell node and  $\nu$  is the local kinematic viscosity [9].

Similarly,  $\frac{u}{u_\tau}$  represents a non-dimensional velocity and expressed as  $u^+$ . The law in the viscous sublayer then boils down to the following equation  $u^+ = y^+$ . In the overlap layer, also called the logarithmic layer, dimensional analysis confirms that velocity is proportional to the logarithm of distance. The velocity profile is then expressed as

$$\frac{U_{avg}}{u_\tau} = \frac{1}{\kappa} \left( \frac{u_\tau y}{\nu} \right) + B \quad (7)$$

where  $\kappa$  is the von Karman constant, a fundamental constant in fluid mechanics and typically 0.414 and  $B$  is an integration constant. This relation is known as the logarithmic law.

Figure 6 (bottom) shows the general features of the turbulent velocity profile.

### 3.2.2 Major Losses

Major losses arises due to friction in the pipe or duct system. It's natural to start with the basics, hence the **Darcy-Wiesbach friction factor**:

$$f = \frac{8\tau_w}{\rho U_{avg}^2} \quad (8)$$

where  $\tau_w$  is given by equation 5.

The friction factor given in equation 9 is needed when calculating the pressure loss:

$$\Delta P_L = f \frac{L}{D} \frac{\rho U_{avg}^2}{2} \quad (9)$$

where  $L$  is the length of the pipe,  $D$  is the hydraulic diameter and  $\frac{\rho U_{avg}^2}{2}$  is the dynamic pressure.

The friction factor in fully developed turbulent flow depends on the Reynolds number and the relative roughness,  $\epsilon/D$ . Relative roughness is the ratio of the mean height of roughness of the pipe to the pipe diameter. Colebrook used data, mainly provided by Prandtl's student, Nikuradse in 1933, to combine data for transition and turbulent flow in smooth as well as rough pipes into the implicit relation we know as the Colebrook equation:

$$\frac{1}{\sqrt{f}} = -2.0 \cdot \log \left( \frac{\epsilon}{3.7D} + \frac{2.51}{Re\sqrt{f}} \right) \quad (10)$$

The Colebrook equation is implicit in  $f$  and thus the determination of the friction factor requires iteration. An approximate explicit relation for  $f$  was given by Haaland in 1983:

$$\frac{1}{\sqrt{f}} = -1.8 \cdot \log \left( \frac{6.9}{Re} + \left( \frac{\epsilon}{3.7D} \right)^{1.11} \right) \quad (11)$$

The results given from this equation are within 2 percent of those obtained from the Colebrook equation. The Moody chart shows that at very large Reynolds numbers,  $> 10^4$ , the friction factors are independent of

the Reynolds number. The Colebrook equation then reduces to the von Kármán equation:

$$\frac{1}{\sqrt{f}} = -2.0 \cdot \log\left(\frac{\epsilon}{3.7D}\right) \quad (12)$$

As a result of the Colebrook equations, the Moody chart was created in order to simply see the correlation between Reynolds number and friction factor with set roughness  $\epsilon/D$  as seen in figure 7.

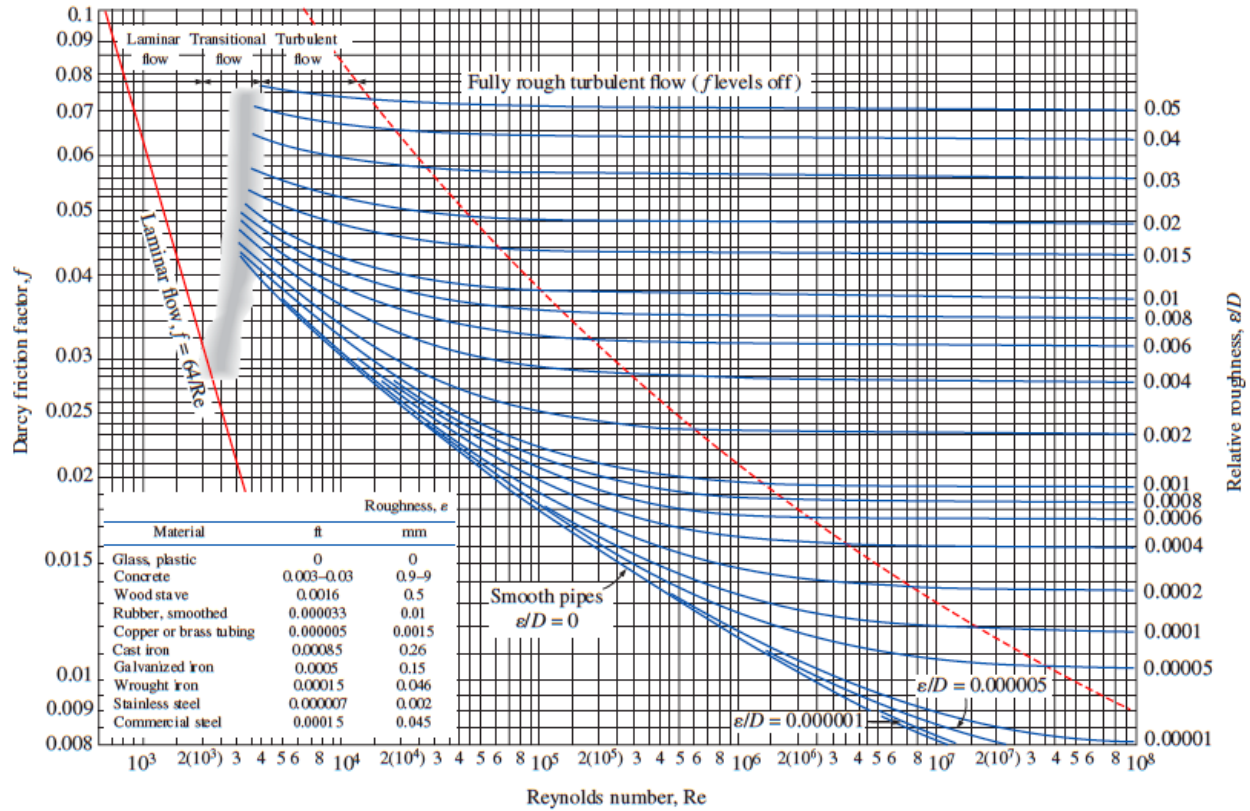


Figure 7: Moody Chart [3]

### 3.2.3 Minor Losses

When the fluid flow is forced in a new direction via e.g. various bends, junctions, expansions and contractions or valves, the fluid flow characteristics are altered and an additional friction factor is to be applied. These factors depend on the geometry of the component, as well as smoothness of the turn or inlet. Minor losses are usually expressed in terms of the **loss coefficient** zeta,  $\zeta$ , defined as;

$$\zeta = \frac{h_L}{U_{avg}^2/(2g)} \quad (13)$$

where  $h_L$  is the additional irreversible head loss in the piping system caused by insertion of the component, defined as  $h_L = \frac{\Delta P_L}{\rho g}$ . While the majority of the irreversible head loss occurs near a component, some of it occurs downstream of the component due to induced swirling turbulent eddies that are produced in the component and continue downstream. It may be natural to think that minor losses occur locally near the minor loss component, but these eddies will have an effect on the flow for several diameters downstream of the component. *“The loss coefficient, in general, depends on the geometry of the component and the Reynolds number. However it is usually assumed to be independent of the Reynolds number”* [3]. Cengel claims that with a large Reynolds number, like most flows have in practice, the loss coefficients including the friction factor, tend to be independent of the Reynolds number. As a result of this assumption, the infamous zeta values are referenced, providing correction factors for various components, irregardless of the Reynolds number as long as the flow is turbulent. Under most practical conditions for internal flow in a circular pipe, the generally accepted value for turbulence is  $Re > 4,000$ . However, the textbook clearly states that these values vary, highly dependent on the manufacturer of the component, and recommend using the manufacturers values if provided. After countless searches online, not a single manufacturer provides information about a pressure loss correction factor for a 90 degree bend, meaning in most cases we are forced to rely on given zeta values.

### 3.2.4 Mach number

The level of variation of density in gas flows and the consequent level of approximation made when modeling gas flows as incompressible depends on the Mach number. For atmospheric air, a pressure change of just 0.01 atm causes a change of 1 percent in the density, while liquids are usually referred to as incompressible substances. In order to consider a gas as incompressible, the density change must remain below 5 percent, requiring a Mach number  $< 0.3$ . The Mach number is defined by  $Ma = \frac{U_{avg}}{c}$ , where  $U_{avg}$  is the average velocity and  $c$  equals the speed of sound in the specific fluid. To find the speed of sound accurate to the fluid, in our case an ideal gas, one can rely on the equation  $\sqrt{\gamma \cdot RT}$ .  $\gamma$  is the specific heat ratio of the fluid and  $R$  is the specific gas constant. Most of the cases in this work are made by taking air as the working fluid. Incompressible flows are thus considered for all cases. This is ensured by keeping the Mach number  $< 0.3$ .

## 3.3 Governing Equations for Fluid Flow

Fluid flows can be defined mathematically using the continuity equation and the momentum equation.

### Conservation of Mass

The balance of mass is expressed by the continuity equation:

$$\frac{\partial \rho}{\partial t} + \vec{\nabla} \cdot (\rho \vec{v}) = 0 \quad (14)$$

where  $\rho$  is the density, that is, the mass per unit volume and  $v$  is the continuum velocity.

### Conservation of Linear Momentum



The time rate of change of linear momentum is equal to the resultant force acting on the continuum:

$$\frac{\partial(\rho\vec{v})}{\partial t} + \vec{\nabla} \cdot (\rho\vec{v} \otimes \vec{v}) = -\vec{\nabla} \cdot (pI) + \vec{\nabla} \cdot \tau + f_b \quad (15)$$

where  $\otimes$ , the outer product denotes the Kronecker product or Identity matrix,  $I$ .  $f_b$  is the resultant of the body forces, such as gravity and centrifugal forces, per unit volume acting on the continuum,  $p$  is the pressure and  $\tau$  is the viscous stress tensor.

### Conservation of Energy:

When the first law of thermodynamics is applied to the control volume, the conservation of energy can be written as:

$$\frac{\partial(\rho E)}{\partial t} + \vec{\nabla} \cdot (\rho E \vec{v}) = f_b \cdot \vec{v} + \vec{\nabla} \cdot (\vec{v} \cdot \tau) - \vec{\nabla} \cdot q + S_E \quad (16)$$

where  $E$  is the total energy per unit mass,  $q$  is the heat flux and  $S_E$  is an energy source per unit volume [10]. Equations 9, 10 and 12 can be expressed in a general transport equation:

$$\underbrace{\frac{\partial \rho \phi}{\partial t}}_{\text{Transient term}} + \underbrace{\nabla \cdot (\rho \vec{u} \phi)}_{\text{Convection term}} = \underbrace{\nabla \cdot (\Gamma \nabla \phi)}_{\text{Diffusion term}} + \underbrace{S_\phi}_{\text{Source term}} \quad (17)$$

where  $\Gamma$  is the diffusion coefficient or diffusivity. The transient term,  $\frac{\partial \rho \phi}{\partial t}$ , accounts for the accumulation of  $\phi$  in the concerned control volume. The advective term,  $\nabla \cdot (\rho \vec{u} \phi)$ , accounts for the transport of  $\phi$  due to the existence of the velocity field (note the velocity  $\vec{u}$  multiplying  $\phi$ ). The diffusion term,  $\nabla \cdot (\Gamma \nabla \phi)$ , accounts for the transport of  $\phi$  due to its gradients. The source term,  $S_\phi$ , accounts for any sources or sinks that either create or destroy  $\phi$ . Any extra terms that cannot be cast into the convection or diffusion terms are considered as source terms. CFD techniques can be used to solve these equations. The objective of all discretization techniques (Finite Difference, Finite Element, Finite Volume, Boundary Element etc.) is to devise a mathematical formulation to transform each of these terms into an algebraic equation. Once applied to all control volumes in a given computational domain, we obtain a full linear system of equations that needs to be solved [11].

### 3.3.1 RANS

Most users of CFD find it adequate using time-averaged properties of the flow, e.g. mean velocities, mean pressures and mean stresses. The computations of turbulent flow are therefore mostly being simulated using Reynolds-average-Navier-Stokes equations, defined as; **Continuity**

$$\frac{\partial \bar{\rho}}{\partial t} + \nabla \cdot (\bar{\rho} \tilde{U}) = 0 \quad (18)$$

## RANS equations

$$\begin{aligned}
\frac{\partial(\bar{\rho})\tilde{U}}{\partial t} + \nabla \cdot (\bar{\rho}\tilde{U}\tilde{U}) &= -\frac{\partial\bar{P}}{\partial x} + \nabla \cdot (\mu\nabla\tilde{U}) + \left[ -\frac{\partial(\overline{\rho u'^2})}{\partial x} - \frac{\partial(\overline{\rho u'v'})}{\partial y} - \frac{\partial(\overline{\rho u'w'})}{\partial z} \right] + S_{Mx} \\
\frac{\partial(\bar{\rho})\tilde{V}}{\partial t} + \nabla \cdot (\bar{\rho}\tilde{V}\tilde{U}) &= -\frac{\partial\bar{P}}{\partial y} + \nabla \cdot (\mu\nabla\tilde{V}) + \left[ -\frac{\partial(\overline{\rho u'v'})}{\partial x} - \frac{\partial(\overline{\rho v'^2})}{\partial y} - \frac{\partial(\overline{\rho v'w'})}{\partial z} \right] + S_{My} \\
\frac{\partial(\bar{\rho})\tilde{W}}{\partial t} + \nabla \cdot (\bar{\rho}\tilde{W}\tilde{U}) &= -\frac{\partial\bar{P}}{\partial z} + \nabla \cdot (\mu\nabla\tilde{W}) + \left[ -\frac{\partial(\overline{\rho u'w'})}{\partial x} - \frac{\partial(\overline{\rho v'w'})}{\partial y} - \frac{\partial(\overline{\rho w'^2})}{\partial z} \right] + S_{Mz}
\end{aligned} \tag{19}$$

## Scalar transport equation

$$\frac{\partial(\bar{\rho}\tilde{\Phi})}{\partial t} + \nabla \cdot (\bar{\rho}\tilde{\Phi}\tilde{U}) = \nabla \cdot (\Gamma_{\Phi}\nabla\tilde{\Phi}) + \left[ -\frac{\partial(\overline{\rho u'\varphi'})}{\partial x} - \frac{\partial(\overline{\rho v'\varphi'})}{\partial y} - \frac{\partial(\overline{\rho w'\varphi'})}{\partial z} \right] + S_{\Phi} \tag{20}$$

where the overbar indicates a time-averaged variable and the tilde indicates a density-weighted or Favre-average variable.

In order to compute turbulent flow using the RANS equations, turbulence models are to be developed. The number of unknowns in the equations above exceeds the number of equations, meaning additional transport equations are to be added depending on the model used.

In this study, the  $\kappa-\epsilon$  model, the  $\kappa-\omega$  model and the RSM model are mostly used. The realizable  $\kappa-\epsilon$  model contains a new transport equation for the turbulent dissipation rate  $\epsilon$ . A critical coefficient of the model  $C_{\mu}$  is expressed as a function of mean flow and turbulence properties, rather than assumed to be constant as in the standard model. This procedure lets the model satisfy certain mathematical constraints on the normal stresses consistent with the physics of turbulence. The concept of a variable  $C_{\mu}$  is also consistent with experimental observations in boundary layers. This model is substantially better than the standard  $\kappa-\epsilon$  model for many applications, and can generally be relied upon to give answers that are at least as accurate. The two-layer realizable  $\kappa-\epsilon$  model will be used in this thesis, granting the added flexibility of an all- $y^+$  wall treatment.

From the standard  $\kappa-\epsilon$  model the  $\epsilon$  transport equation was transformed into the  $\kappa-\omega$  model by adding an additional non-conservative cross-diffusion term containing the dot product  $\Delta k \cdot \Delta \omega$ . By further modifying the linear constitutive equation, the SST (shear-stress transport)  $\kappa-\omega$  model arises. The SST model has seen fairly wide application in the aerospace industry, where viscous flows are typically resolved, and turbulence models are applied throughout the boundary layer.

The Reynolds Stress Transport Model, from now on referred to as RSM, have the potential to predict complex flows because the transport equations for the Reynolds stresses naturally account for the effects of turbulence anisotropy, streamline curves, swirl rotation and high strain rates. RSM is more computationally expensive, mainly because the model solves the actual stresses and all the components of the turbulent transport in contrast to eddy-viscosity two-equation models such as  $\kappa-\epsilon$  and  $\kappa-\omega$  who solves the stresses as a mean rate plus a fluctuating component.

## **3.4 CFD Technique & STAR-CCM+**

Computational fluid dynamics is the analysis of systems involving fluid flow, heat transfer and associated phenomena such as chemical reactions by means of computer-based simulation [8]. Increasingly CFD is becoming a vital component in the design of industrial products and processes. CFD codes are structured around the numerical algorithms that can tackle fluid flow problems. In order to provide easy access to their solving power all commercial CFD packages include sophisticated user interfaces to input problem parameters and to examine the results, including the main elements following in the next three sections.

### **3.4.1 Pre-processor**

When simulating a CFD problem, certain input values must be defined. These inputs include definition of the geometry, called the computational domain, grid generation dividing the domain into control volumes or mesh, selection of the physical and chemical phenomena that need to be modeled, definition of fluid properties and specification of appropriate boundary conditions.

The accuracy of a CFD solution is governed by the number of cells in the mesh grid. Optimal meshes are often non-uniform, finer in areas where large variations occur from point to point and coarser in regions with relatively little change. Over 50% of the time spent in industry on a CFD project is devoted to the definition of the domain geometry and grid generation. Up-to-date pre-processors give the user access to libraries of material properties for common fluids and a facility to invoke special physics and chemical process models.

### **3.4.2 Solver**

In most well-established CFD codes the finite volume method is central. The numerical algorithm consists of integration of the governing equations of fluid over all the finite control volumes of the domain, discretization meaning conversion of the resulting integral equations into a system of algebraic equations and solution of the algebraic equations by an iterative method.

### **3.4.3 Post-processor**

When presenting results given by the solver step, most CFD packages are equipped with versatile data visualization tools. These include, but are not limited to, vector and scalar plots, geometry and grid display, surface plots in both 2D and 3D and particle tracking. This opens the door for communicating ideas and results to the non-specialist e.g. investors.

STAR-CCM+ is a comprehensive simulation tool which offers modulation of a range of physics phenomena including fluid mechanics. In order to solve multiple equations in some cases thousands of times during a simulation run, STAR-CCM+ have requirements for the computer system.

Hardware Component	Workstations	Laptops
Processor	2.4 GHz CPU with at least 4 cores per CPU (to allow client and server to work in separate spaces and to run in parallel).	No minimum speed for the CPU. However, you are advised to have at least 2 cores per CPU (so that the client and server to work in separate spaces). Higher number of cores permit running in parallel.
Memory	2 GB of memory per core.	2 GB of memory per core.
Disk Space	9 GB of free disk space (more space is required to save simulations).	9 GB of free disk space (more space is required to save simulations).
Graphics Card	Dedicated graphics hardware that has 3D capability, z-buffer and translucency.	Dedicated graphics hardware that has 3D capability, z-buffer and translucency. Integrated graphics chipsets are not recommended.

Figure 8: System Requirements for using STAR-CCM+ [12]

There has been a combination of computers being used when running simulations. Some of them have been done on computers provided by the campus, which meets the set requirements with ease, and some of them on one of our personal computers. This computer has an Intel i3 7100U CPU with duo 2.40 GHz cores processor with a total memory of 6 GB. It has been able to run all simulations, but the clock time has varied depending on the scale of the geometry. Run times are presented in relevant cases. The mathematical models that describe the physics of continua are derived from fundamental laws that express conservation principles. In terms of conservation laws, this thesis will present results using a Eulerian approach, where the given volume represents a portion of space where material can flow through [10].

## 4 Method

### 4.1 Geometry

In order to design our geometry in STAR-CCM+ within the validation thesis, a CAD model was implemented. The CAD tool includes a sketching function, where a circle with a certain diameter was drawn to match the Reynolds number, and extruded twenty times the diameter to properly illustrate a fully developed flow (see figure 9).

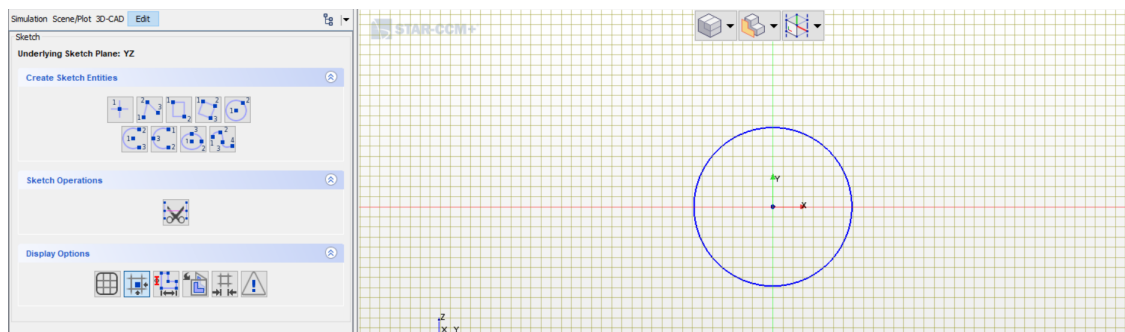


Figure 9: Making sketches in Star CCM+ [10]

## 4.2 Mesh

When generating mesh it is important to define the position in or on the geometry where it is expected to have the greatest change in e.g. pressure, energy or velocity, depending on the case. This is important regarding the capacity of the working computer as a very high cell count demands massive computer power, which can ultimately result in a running time of hours or even days. When pinpointing the position of interest, one can use a finer mesh at that point and a coarser mesh on the remaining computational domain.

## 4.3 Boundaries

When selecting boundary conditions in Star CCM+, it is necessary to make parts from the original geometry. For example a straight pipe has normally an inlet, an outlet and wall boundary conditions. When simulating pressure loss through a pipe, we use a *velocity inlet* at the pipe inlet and *pressure outlet* condition at the pipe outlet. The remaining pipe in between are defined as a no slip wall, making it possible to alter the wall characteristics.

## 4.4 Wall Treatment

To resolve the near wall flow accurately, mesh modeling uses a tool called prism layer mesh. Prism layers are required in modeling turbulence because of the forces from the wall acting on a fluid causes effects of drag and pressure drop. By increasing the number of nodes near the wall and in general, the realization of the cross-stream provides enhanced stream-wise resolution. When the walls are smooth, the shear stress at the surface is transmitted to the flow via the viscous sublayer and needs to be accurately modeled to resolve the velocity and temperature gradients normal to the wall. Using a prism layer mesh allows you to resolve the viscous sublayer directly if the turbulence model supports it. This is where the  $y^+$  becomes considerable.  $y^+$  is often used to describe how coarse or fine a mesh is for a particular flow pattern.

To get the correct validation for our thesis,  $y^+$  is important in order to obtain the right friction factor related to the Moody chart. The  $y^+$  value was adjusted by altering the thickness of the wall-adjacent cell node. Different  $y^+$  approaches of STAR-CCM+ is illustrated in figure 10.

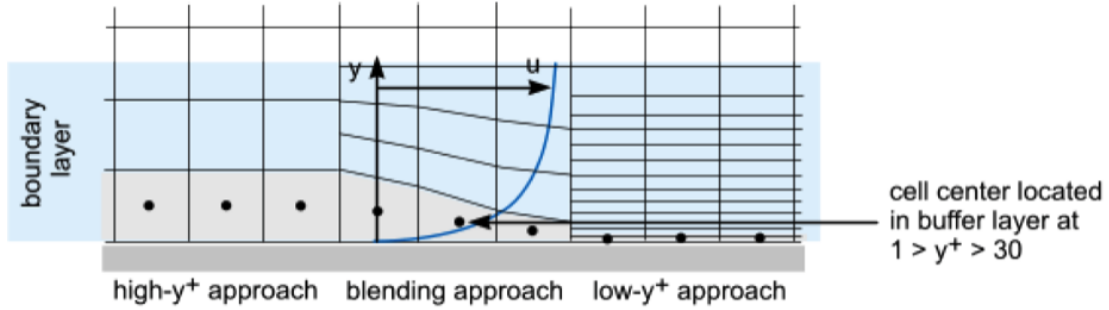


Figure 10:  $y^+$  approach [10]

Initially, our goal was to keep  $y^+ < 5$  when dealing with a pipe where the walls are smooth to ensure that the viscous sublayer gets properly resolved. However, three of four  $y^+$  values were above 5, to attain the correct results. When dealing with wall roughness,  $y^+$  is recommended in the range 25 to 30. Then, the first wall centroid falls within the buffer region of the boundary layer. A blending function is then used to calculate turbulence quantities such as dissipation, production, and stress tensor. However, that wasn't the approach that gave us the results we wanted. We learned that the Reynolds number also plays an important role in determining which  $y^+$  is acceptable for each case. To obtain the right friction factor, we noticed an increasing value of the Reynolds number led to a higher value of  $y^+$ , with some exceptions.

## 4.5 Roughness Modeling

Roughness in pipes can result in disturbance to the velocity field and significantly change the flow behavior. Its physical appearance can be viewed as small obstacles at the wall boundary of any given component.

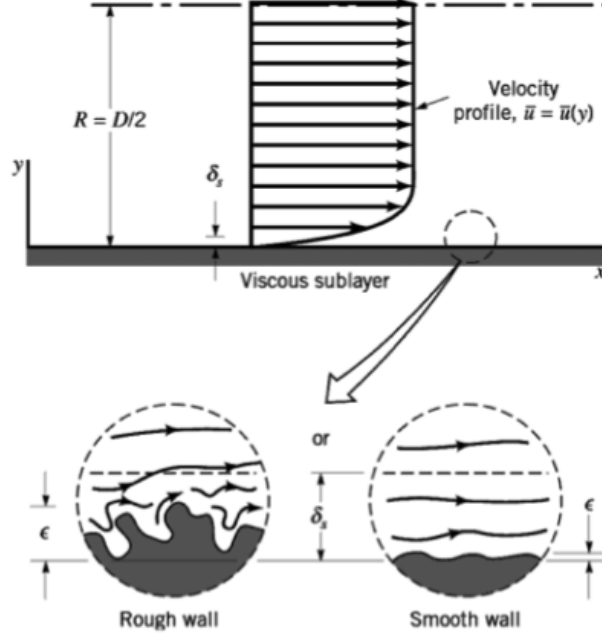


Figure 11: Roughness [13]

Figure 11 shows the roughness effects in the viscous sublayer for a smooth and a rough wall.

To account for the effects of pipe roughness in a turbulent flow, some correction factors are generally used to properly illustrate how the roughness is affecting the fluid flow. The *sand-grain* roughness is a length parameter and usually expressed as  $\epsilon$ . It is typically quite small (0-0.1m). In deciding upon a wall treatment for a situation where the pipe is rough, the non-dimensional sand-grain roughness, also called the roughness Reynolds number,  $R^+$ , has to be considered.  $R^+$  represents the fluid properties of a viscous flow. The definition of  $R^+$  is:

$$R^+ = \frac{\epsilon u_\tau}{\nu} \quad (21)$$

When dealing with roughness,  $y^+$  is recommended to exist in the range of 25-30. Here, the logarithmic law for a rough surface yields:

$$\frac{U_{avg}}{u_\tau} = \frac{1}{\kappa} \left( \frac{u_\tau y}{\nu} \right) + B - \Delta B(R^+) \quad (22)$$

where  $\Delta B$  is a function of  $R^+$ , the roughness function.  $\Delta B$  exists in three different regions. The smooth region where  $R^+ < 2.25$ , the transitional  $2.25 < R^+ < 90$ , and the fully rough regime where  $R^+ > 90$  [14]. In most of our CFD simulations,  $R^+$  was found to be in the transitional regime. When we are in the fully rough regime the sublayer gets irrelevant, and the logarithmic profile can stop intersecting with the assumed linear profile in the sublayer. If these curves do not intersect in the transitional roughness regime  $R_{smooth}^+ > R^+ > R_{rough}^+$ , STAR-CCM+ uses the logarithmic profile with requirements that  $u^+$  never falls below zero. When this condition is violated, STAR-CCM+ limits the roughness height locally such that  $R^+ = y^+$  when  $y^+$  becomes less than  $R^+$ . [10].

## 5 Problem Setup

When initially running the STAR-CCM+ software we found it helpful to start with the basics using tutorials. STAR-CCM+ offers an extensive database, including a user guide, theory and tutorials, being greatly appreciated in our learning process. In order to implement a CAD model, a sketch was to be made. A circle was created in the internal sketching tool matching the geometry of interest, to begin with a straight pipe. After designing appropriate parts to our body, inlet, outlet and wall, we assigned boundaries to the parts, velocity inlet and pressure outlet. We chose what appeared to be satisfactory surface and volume mesh, using trimmer mesh, surface re-mesher and prism layer mesh functions. We defined the physics of the fluid as incompressible air and left the wall roughness as smooth. We chose the  $\kappa - \epsilon$  solver and started running our first case with a maximum number of iterations at 1000. In order to calculate the Darcy-Weisbach friction factor, a field function was created in STAR-CCM+ attaining the equation  $C_f = \frac{8\tau_{wall}}{\rho v^2}$ . When comparing the results of pressure loss through our geometry with the Haaland and Colebrook equations and also the Moody chart, the results were not satisfactory. We started from scratch, redefining our mesh, adjusting the  $y^+$  value, the prism layer count, thickness and stretching, made sure our cell count was not too high and kept an eye on the Mach number, making sure it was  $< 0.3$ . After several runs, residuals show converging behavior and the results were found to be comparable with the classical formulas.

### 5.1 Straight Pipe

In order to validate the final results given by Star CCM+, cases using a straight pipe as a geometry was simulated and run with different Reynolds numbers and wall roughnesses. In order to alter the Reynolds number, changes were made in the geometry, increasing both diameter and length of the pipe when aiming for increased Reynolds number. The simulations were run with incompressible air as fluid in a smooth pipe with circular cross section.

The range of these values were chosen to also compare with the experiments presented in the European Report [4]. The length of the pipes were determined by multiplying the diameter at work with 20. In addition, three levels of relative roughness were run to compare with the Haaland and Colebrook equations (the Moody chart), presented under the Results section. Using a simple geometry of a straight pipe,



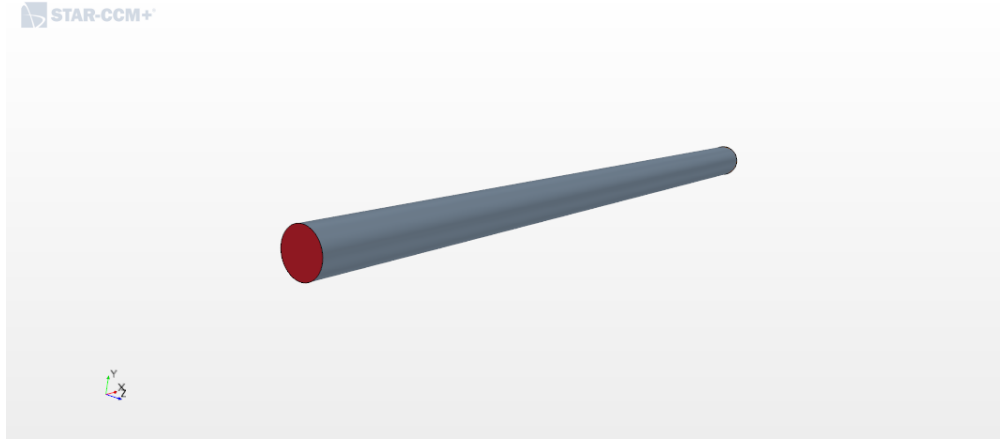


Figure 12: Geometry of a straight pipe, STAR-CCM+

when running simulations, physics and boundary condition selections are similar for all the different Reynolds numbers. The mesh selections and other properties that vary are shown in separate tables for each case. Figure 12 shows the CAD geometry for the straight pipe case.

Parameter	Menu Properties	Selection/Value inputted
<b>Physics Selection</b>	Time	Steady
	Material	Gas
	Flow	Segregated Flow
	Equation of State	Constant Density
	Viscous Regime	Turbulent
	RANS	K-Epsilon
<b>Boundary Condition Selection</b>	Inlet	Inlet Velocity
	Outlet	Outlet Pressure
	Wall	Wall
	Turbulent Intensity	10%
	Turbulence Specification	Intensity + Length Scale
	Turbulent Length Scale	3.8% of Hydraulic Diameter
	Turbulent Velocity Scale	10% of Inlet Velocity
	Temperature	300K
Wall Condition	No Slip	

Table 1: Properties used for all cases

Table 1 describes the input data for all following cases including the roughness model used, material selection and boundary conditions

<b>Properties</b>	<b>Re 50,000</b>	<b>Re 100,000</b>	<b>Re 200,000</b>	<b>Re 500,000</b>
Mesh Type	TSP	TSP	TSP	TSP
Base Size	20 mm	20 mm	15 mm	20 mm
Prism Layer Thickness	39%	40%	25%	50%
Number of Layers	6	6	4	6
Prism Layer Stretching	2.0	1.5	1.5	2.0
Cell Count	24,648	107,414	42,000	43,120
$Y^+$	1.9	5.3	13.2	8.3
Mach	0.029	0.029	0.058	0.115

Table 2: Properties used for Case 1, smooth pipe. TSP represents using the trimmer mesh, the surface re-mesher and prism layer mesher.

Table 2 shows the properties used for the smooth pipe. The cell count for  $Re = 10^5$  is larger compared to the other cases because of the fine mesh close to the walls as seen in figure 13.

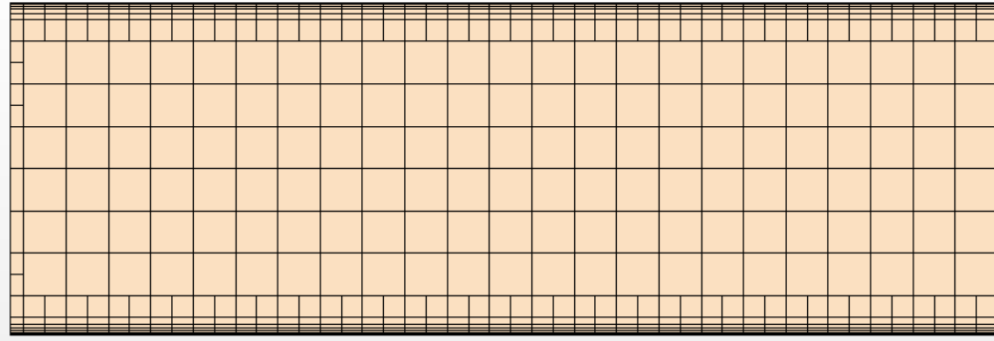


Figure 13: Mesh in a plane section used for Re 100,000 with no roughness

Tables 3, 4 and 5 show the properties used for the rough pipe cases. In all cases the  $y^+$  was accounted for, and modified to obtain a satisfactory value for the friction factor. The base size of the cells are kept at 10 or 20 mm for all cases.

<b>Properties</b>	<b>Re 50,000</b>	<b>Re 100,000</b>	<b>Re 200,000</b>	<b>Re 500,000</b>
Mesh Type	TSP	TSP	TSP	TSP
Base Size	10 mm	20 mm	20 mm	20 mm
Prism Layer Thickness	42%	40%	44.5%	50%
Number of Layers	4	4	6	4
Prism Layer Stretching	1.0	1.0	1.1	1.0
Cell Count	80,960	80,328	108,899	33,712
$y^+$	17.0	30.2	32.9	131.3
Mach	0.029	0.029	0.058	0.115
$R^+$	0.3	0.5	0.9	2.1

Table 3: Properties used for Case 2,  $\epsilon/D = 0.0001$ .

<b>Properties</b>	<b>Re 50,000</b>	<b>Re 100,000</b>	<b>Re 200,000</b>	<b>Re 500,000</b>
Mesh Type	TSP	TSP	TSP	TSP,
Base Size	10 mm	20 mm	20 mm	20 mm
Prism Layer Thickness	45%	67%	20.5%	16.8%
Number of Layers	4	1	1	1
Prism Layer Stretching	1.0	1.0	1.0	1.0
Cell Count	81,577	39,858	11,376	24,304
$y^+$	18.7	206.0	122.0	200.8
Mach	0.029	0.029	0.058	0.115
$R^+$	1.3	2.5	4.8	11.9

Table 4: Properties used for Case 3,  $\epsilon/D = 0.0005$ .

Figures 14 and 15 shows the mesh used for two of the cases. Figure 14 shows a finer mesh at the walls, but both cases yield good residuals (see Appendix A).

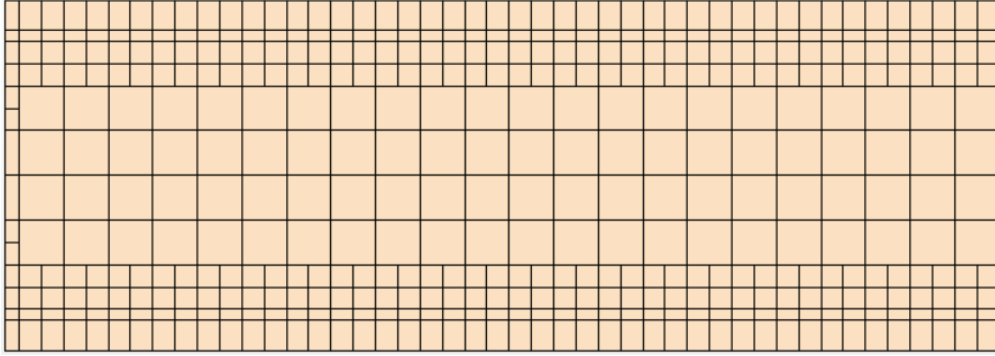


Figure 14: Mesh used for Re 100,000 with  $\epsilon/D = 0.0005$

<b>Properties</b>	<b>Re 50,000</b>	<b>Re 100,000</b>	<b>Re 200,000</b>	<b>Re 500,000</b>
Mesh Type	TSP	TSP	TSP	TSP
Base Size	20 mm	20 mm	20 mm	20 mm
Prism Layer Thickness	91.5%	52%	10%	20%
Number of Layers	2	1	1	1
Prism Layer Stretching	1.0	1.0	1.0	1.0
Cell Count	6,336	44,672	11,376	24,304
$y^+$	140.7	165.7	66.3	250.1
Mach	0.029	0.029	0.058	0.115
$R^+$	2.4	4.5	9.6	22.6

Table 5: Properties used in Case 4,  $\epsilon/D = 0.0009$ .

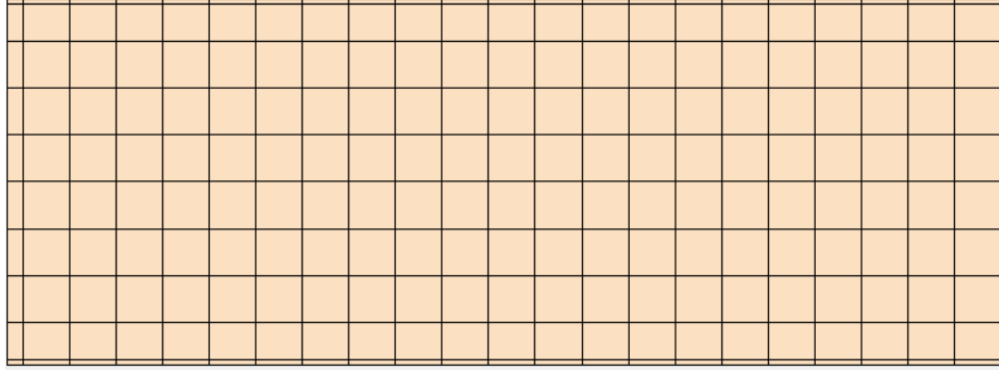


Figure 15: Mesh used for Re 200,000 with roughness  $\epsilon/D = 0.0009$

## 5.2 90 Degree Bend

When running simulations using a 90° bend, the cases are based on previous experimental setup reported by Salehi, Sleiti and Idem [5] and also by Koch [4]. The ultimate goal of these simulations are to confirm the effects of varying both Reynolds number and the diameter when calculating the pressure loss. We made sure that every residual went below  $10^{-6}$ .

To properly resolve the sublayer when dealing with bends, the number of prism layers were increased for increasing Reynolds numbers. When varying the diameter, we first ran simulations using the RSM model. Then, we compared the results we attained, with the  $\kappa - \epsilon$  model. The RSM model gave satisfactory residuals while the  $\kappa - \epsilon$  model did not. The exact same mesh was used in each of the cases. When varying the Reynolds number, the diameters used were 150mm, 200 mm and 250mm. Incompressible flow were set for all cases. Figure 17 shows how the CAD model for 90 degree bend was made, by extruding the sketch in figure 16.

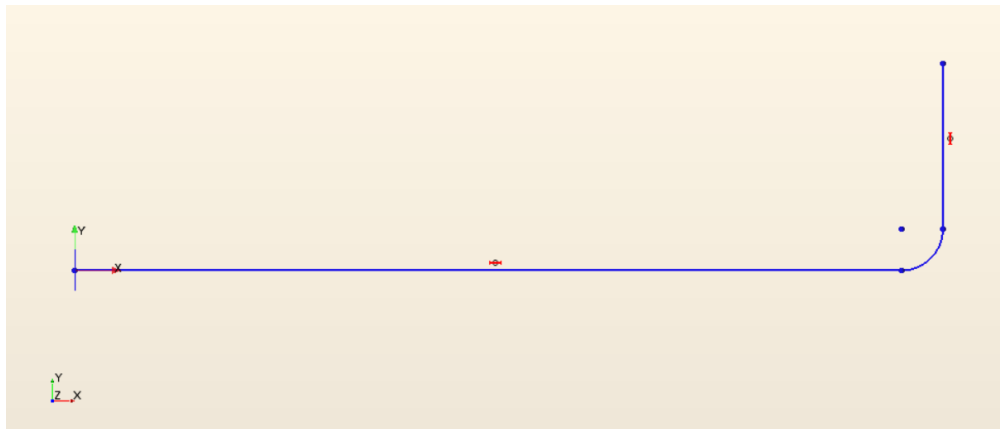


Figure 16: Sketch of 90 degree bend

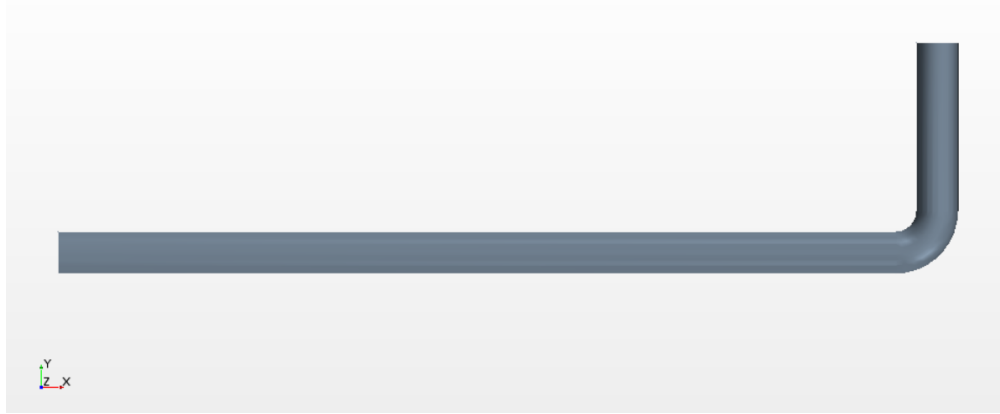


Figure 17: Geometry of a 90 degree bend, STAR-CCM+

Table 6, 7 and 8 show the input data for the varying diameter cases, with constant Reynolds numbers at  $Re=10,000$ ,  $Re=50,000$  and  $Re=150,000$ . As the geometry now is more complex, it has been added number of iterations before convergence and the runtime before reaching residuals values at  $< 10^{-6}$ . With given geometry and cell count, cases are bound to require more time. The following tables in this sections contains NPL and PLT, respectively number of prism layers and prism layer thickness.

<b>Varied diameter run with <math>Re=10,000</math> and RSM model</b>						
Diameter [mm]	Base size [mm]	Cell count	NPL	PLT	Run time	Iterations
100	20	65,259	8	30 %	2.3 min	391
125	20	88,039	8	30 %	3.7 min	450
150	20	111,235	8	40%	4.7 min	440
175	20	113,053	8	40%	5.1 min	495
200	20	109,107	8	50%	4.5 min	479
225	20	106,421	8	50%	4.8 min	456
250	20	137,439	8	60%	5.8 min	484
275	20	166,489	8	60%	8.0 min	551
300	20	201,452	8	70%	12.4 min	615
400	20	372,846	8	70%	25.3 min	726

Table 6: Properties used for varying diameter with  $Re=10,000$

<b>Varied diameter run with Re=50,000 and RSM model</b>						
Diameter [mm]	Base size [mm]	Cell count	NPL	PLT	Run time	Iterations
100	20	65,259	8	30 %	2.5 min	433
125	20	88,039	8	30 %	4.0 min	495
150	20	111,235	8	40%	7.9 min	833
175	20	113,053	8	40%	8.2 min	783
200	20	109,758	8	30%	4.7 min	471
225	20	106,421	8	50%	8.8 min	961
250	20	137,439	8	60%	10.1 min	832
275	20	166,489	8	60%	16.2 min	1117
300	20	201,452	8	70%	21.8 min	1,180
400	20	372,846	8	70%	22.2 min	655

Table 7: Properties used for varying diameter with Re=50,000

<b>Varied diameter run with Re=100,000 and RSM model</b>						
Diameter [mm]	Base size [mm]	Cell count	NPL	PLT	Run time	Iterations
100	20	78,243	10	30 %	4.0 min	595
125	20	104,975	10	30 %	4.0 min	426
150	20	132,303	10	40%	7.9 min	632
175	20	134,409	10	40%	11.4 min	935
200	20	129,743	10	50%	9.1 min	779
225	20	126,481	10	50%	7.0 min	650
250	20	162,963	10	60%	13.3 min	872
275	20	196,833	10	60%	16.6 min	1,000
300	20	236,243	10	100%	22.0 min	1,082
400	20	492,848	12	120%	31.8 min	730

Table 8: Properties used for varying diameter with Re=100,000

Tables 9, 10 and 11 show properties used for the varying Reynolds number cases with constant diameters at  $d/\text{mm}=150$ ,  $d/\text{mm}=200$  and  $d/\text{mm}=250$ . All cases are run using a smooth 90 degree bend. In order to achieve satisfactory residuals, some of the lower Reynolds number cases required a decreased number of prism layers.

<b>Varied Reynolds number run with <math>d/\text{mm}=150</math> and RSM model</b>						
Reynolds number	Base size [mm]	Cell count	NPL	PLT	Run time	Iterations
10,000	20	110,449	8	40 %	7.3 min	472
50,000	20	130,611	10	60 %	10.4 min	940
100,000	20	130,968	10	50%	14.5 min	1,201
150,000	20	130,968	10	50%	9.3 min	791
200,000	20	131,373	10	40%	5.9 min	533
250,000	20	131,373	10	40%	6.1 min	541
300,000	20	131,373	10	40%	5.1 min	461
350,000	20	131,373	10	40%	6.6 min	587
400,000	20	131,373	10	40%	7.9 min	701
500,000	20	131,373	10	40%	5.6 min	505

Table 9: Properties used with varying Reynolds numbers and  $d/\text{mm}=150$

<b>Varied Reynolds number run with d/mm=200 and RSM model</b>						
Reynolds number	Base size [mm]	Cell count	NPL	PLT	Run time	Iterations
10,000	20	117,230	9	40 %	10.0 min	838
50,000	20	117,230	9	40 %	8.1 min	767
100,000	20	127,024	10	50%	8.8 min	814
150,000	20	127,024	10	50%	8.8 min	813
200,000	20	127,024	10	50%	7.9 min	737
250,000	20	127,024	10	50%	6.9 min	648
300,000	20	127,024	10	50%	5.9 min	540
350,000	20	127,024	10	50%	6.1 min	503
400,000	20	127,024	10	50%	5.2 min	486
500,000	20	127,024	10	50%	5.7 min	501

Table 10: Properties used with varying Reynolds numbers and d/mm=200

<b>Varied Reynolds number run with d/mm=250 and RSM model</b>						
Reynolds number	Base size [mm]	Cell count	NPL	PLT	Run time	Iterations
10,000	20	103,279	6	60 %	4.2 min	450
50,000	20	150,415	10	60 %	11.0 min	877
100,000	20	150,415	10	60%	10.3 min	810
150,000	20	150,415	10	60%	9.9 min	783
200,000	20	150,415	10	60%	9.8 min	777
250,000	20	150,415	10	60%	9.5 min	727
300,000	20	150,415	10	60%	10.1 min	728
350,000	20	150,415	10	60%	6.6 min	514
400,000	20	150,415	10	60%	7.0 min	534
500,000	20	150,931	10	40%	7.2 min	563

Table 11: Properties used with varying Reynolds numbers and d/mm=250

Figure 18 shows a typical mesh in a plane section used for one of the pipe bend cases. It shows a polyhedral mesh network, which is used in all of the bend cases.

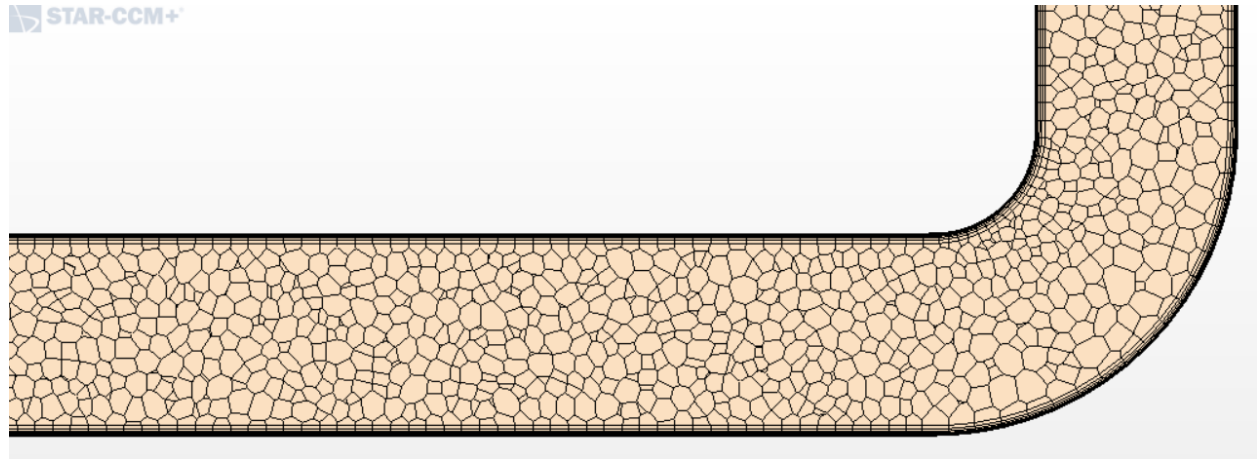


Figure 18: Mesh used for bend with Re 400,000 and diameter 200mm

### 5.3 Matlab

When presenting the results, we wanted to show a plot including our own values compared to both the Haaland and Colebrook equations. In order to do this suitable, a Matlab script is made. By implementing the equations, given the range of Reynolds numbers and friction factors, and values found by STAR-CCM+, we were able to present our results in a fashionable way.



# 6 Results and Discussion

In addition to results presented as digits and plots, various visualizations provided by STAR-CCM+ offer to show planes of flow behavior at positions of interest based on the geometry. The visualizations can contribute to the understanding of the results to the non-specialist and offer a simplified way of interpreting what is really happening during a fluid flow through a domain. Figure 19 shows a typical plane containing the behavior of velocity and pressure through a straight pipe.

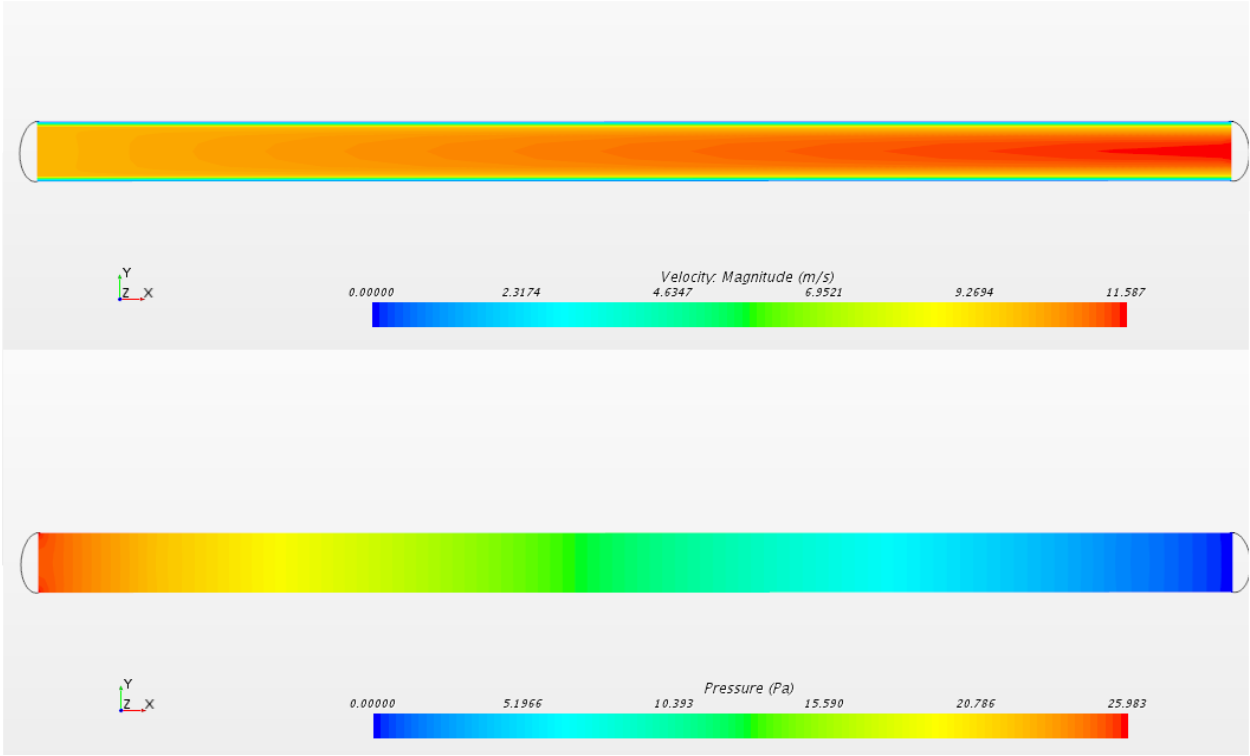


Figure 19: A typical velocity and pressure plane

## 6.1 Straight Pipe

The results regarding the straight pipe are mainly to validate STAR-CCM+'s ability to compute pressure loss in a circular pipe by comparing total pressure loss calculated by the software to the Haaland equation, the Colebrook equation (the Moody chart). Keeping in mind eventual errors including user errors, due to the complexity of the program, all results are accompanied by relevant input values and mathematical work. All values shown in this section have converging residuals in STAR-CCM+.

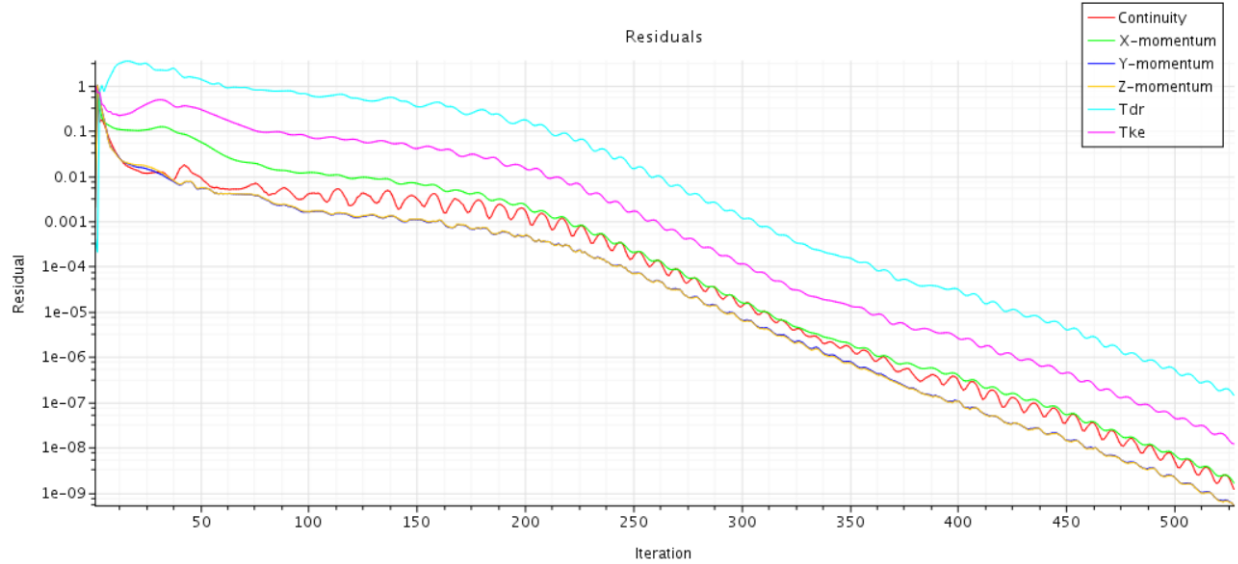


Figure 20: Residuals for Re 50,000 in smooth pipe

Figure 20 shows the residuals for Re=50,000 in a smooth pipe, converging beyond the point  $10^{-6}$ . Residuals for cases with straight pipes with rough walls are given in appendix A. Our initial work disclosed simulations in a smooth, straight pipe followed by three runs with various wall roughnesses. All cases were run with four different Reynolds numbers, to acquire sufficient data for a full validation.

<b>Unmodified <math>y^+</math> with Roughness <math>\epsilon/D = 0.0009</math></b>		
Reynolds Number	Turbulence Model	Percentage of Error
50,000	$\kappa - \epsilon$	6.9
	$\kappa - \omega$	6.5
	RSM	5.3
100,000	$\kappa - \epsilon$	13.4
	$\kappa - \omega$	9.1
	RSM	12.3
200,000	$\kappa - \epsilon$	3.8
	$\kappa - \omega$	6.8
	RSM	14.9
500,000	$\kappa - \epsilon$	27.7
	$\kappa - \omega$	19.7
	RSM	12.2

Table 12: Percentage of error with unmodified  $y^+$

When running the simulations with unmodified  $y^+$  and with roughness  $\epsilon/D = 0.0009$  for the three different models, we cannot find a pattern other than the apparent increase in error relative to the increase of the Reynolds number (see table 12). The  $y^+$  range in these cases are  $25 \leq y^+ \leq 30$ .

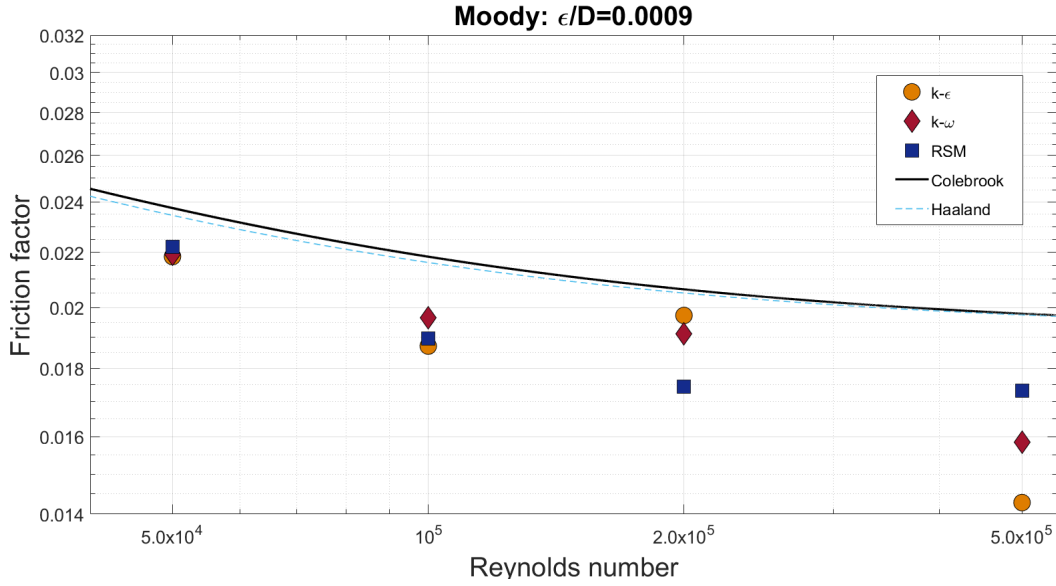


Figure 21: Reynolds number vs friction factor including comparing results

Table 12 and figure 21 presents the results given varying the turbulence model with the four Reynolds numbers from previous cases. By keeping the  $y^+$  unmodified, the results, if nothing else, show great variation in simulating the flow through a straight pipe and appear to increase the error relative to the increase of Reynolds number for all models. A further detailed study can be done in the future to comprehensively conclude the behavior of these models.

Modified $y^+$ with $\kappa - \epsilon$		
Reynolds Number	Roughness $\epsilon/D$	Percentage of Error
50,000	Smooth	0.5
	0.0001	0.7
	0.0005	0.2
	0.0009	0.6
100,000	Smooth	0.08
	0.0001	0.1
	0.0005	0.4
	0.0009	0.02
200,000	Smooth	0.1
	0.0001	0.2
	0.0005	0.2
	0.0009	0.02
500,000	Smooth	0.3
	0.0001	0.01
	0.0005	0.01
	0.0009	0.1

Table 13: Percentage of error with modified  $y^+$

The percentage of error shown in the tables are relative to the Haaland equation. Table 13 presents results given from sixteen separate cases, varying Reynolds number and wall roughness. They have all been simulated using the  $\kappa - \epsilon$  model and the values of  $y^+$  have been modified in the range of  $17 \leq y^+ \leq 250$  to each case to ensure a low percentage of error, here consistently below 0.7%. When comparing these results to the ones reported by Salehi [5], their percentage of error was less than 3% in their case for Re higher than 250,000 for a smooth pipe, using the  $\kappa - \epsilon$  model, when comparing the results with the Colebrook equation. For a rough pipe with  $\epsilon/D = 0.0009$  their results show accuracy within 7% error for Re higher 250,000 and within 12% error for Re lower than 250,000. One might want to interpret these results as if confirming the accuracy of STAR-CCM+'s way of calculating fluid flow through a circular pipe.

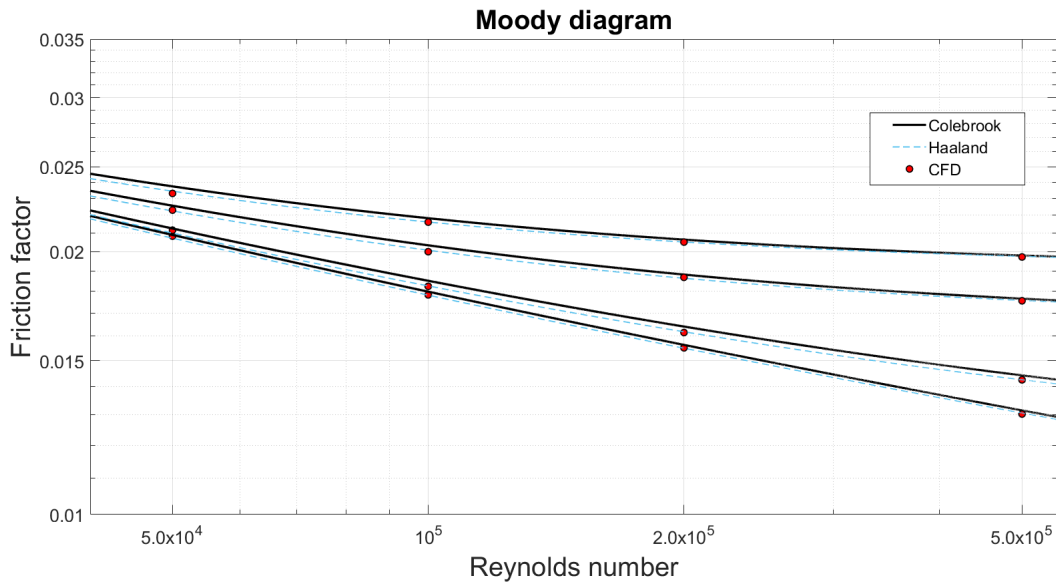


Figure 22: Reynolds number vs friction factor including comparing results

Figure 22 is a plot generated from Matlab. This compares the simulated results with both the Colebrook and the Haaland equations. Along with the table showing the percentage of error, we can conclude that the best results were given with modified  $y^+$  values using the  $\kappa - \epsilon$  model.

## 6.2 90 Degree Bend

When interpreting the results from the bend cases, research papers given by, among others, Koch and Salehi are used to compare. Salehi's research include results using the RSM turbulence models with a range of errors between 4 and 16%. Their conclusions included recommendations for turbulence model selections for both smooth and rough pipes along with recommended range of  $y^+$ . For smooth duct walls they recommend using the  $\kappa - \epsilon$  turbulence model for  $Re > 100,000$  flow in straight duct with enhanced wall treatment grid requirements of  $3 \leq y^+ \leq 4$ . For rough duct walls they recommend using the  $\kappa - \epsilon$  turbulence model for  $Re > 100,000$  flow in straight duct with wall functions grid requirements of  $25 \leq y^+ \leq 30$ . They add that

for all geometries with rough duct walls you should use wall functions grid requirements of  $25 \leq y^+ \leq 30$ . As for elbows they recommend using the RSM turbulence models. [5].

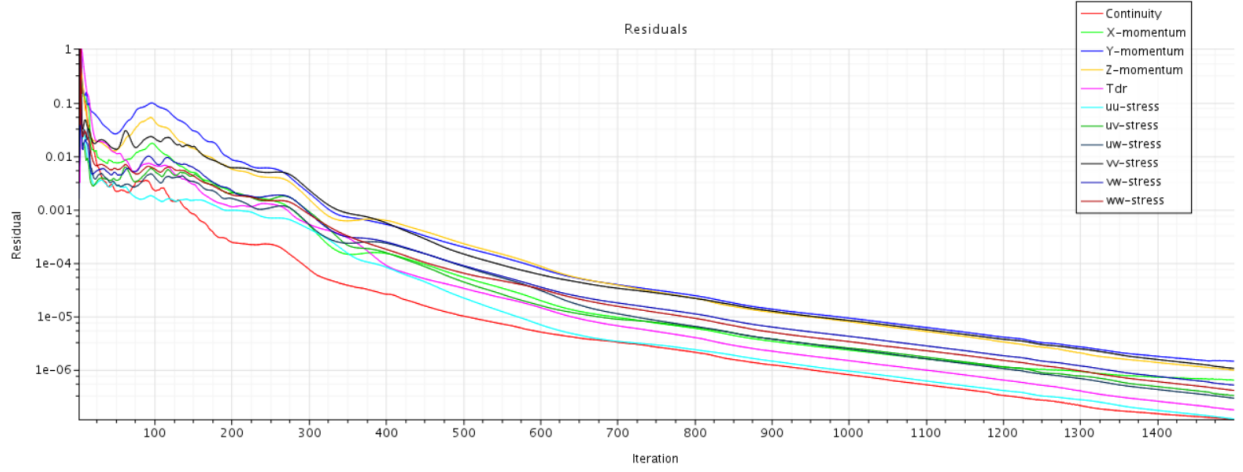


Figure 23: Residuals for bend with Re 400,000

Figure 23 shows the residuals for bend with Re=400,000.

When varying the Reynolds number, the following results are based on a relative zeta value, with a reference value at Re=200,000. Calculation of the reference value are taken as an average of three zeta values for Re=200,000, and is found to be 0.266. The correction factor  $C_{Re}$  is calculated using the following formula:

$$C_{Re} = \frac{\zeta}{\zeta_*} \quad (23)$$

where  $\zeta_*$  is the reference value at a chosen Reynolds number. We report  $C_{Re}$  in the following texts and compare the results with the available literature.

### 6.2.1 Varying Diameter

Zeta values			
d/mm	Re=10,000	Re=50,000	Re=100,000
100	0.511	0.356	0.289
125	0.516	0.362	0.289
150	0.54	0.363	0.289
175	0.531	0.367	0.287
200	0.516	0.384	0.28
225	0.517	0.359	0.277
250	0.533	0.358	0.277
275	0.55	0.371	0.285
300	0.583	0.386	0.293
400	0.6	0.419	0.316
<b>Deviation</b>	0.089	0.063	0.039

Table 14: Zeta values with varying diameter

Referring to figure 24, it appears that the zeta value is in some fashion independent of the diameter. Based on read reports on this issue [4], these CFD results are quite different from the results in Koch. To verify these results, a comparison to the Reynold vs zeta was made. In this case we ran simulations with a variation of diameters and made plots for three different Reynolds numbers. These three points where divided by  $\zeta_*$  and plotted against the varying Reynolds curve. With some deviation from the original curve. We know that every simulation comes with a simulation error, so we still believe that these points matches the Reynolds plot, because of the pattern of the location of the points. This reveals that zeta is predominally a function of the Reynolds number. However, the diameter may play a role in the calculation of the zeta value.

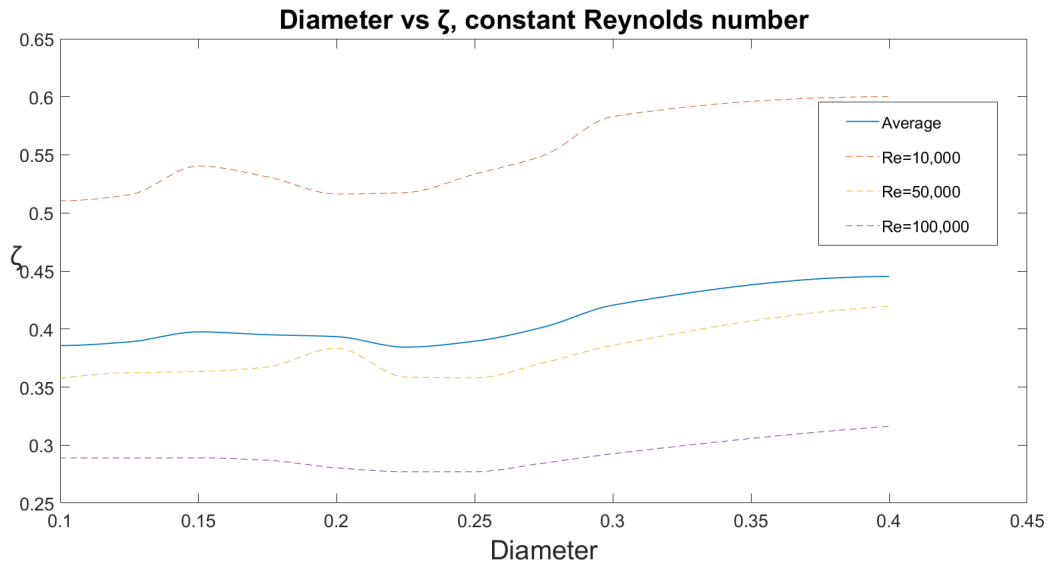


Figure 24: Zeta values plot with varying diameter

### 6.2.2 Varying Reynolds Number

When varying the Reynolds numbers in the range from  $Re=10,000$  to  $Re= 500,000$  in ten cases, each case was run with three different diameters in order to compare the deviation to one another.

$C_{Re}$ values with varying Reynolds number			
Reynolds number	d/mm=150	d/mm=200	d/mm=250
10,000	1.98	1.90	2.22
50,000	1.38	1.38	1.39
100,000	1.17	1.20	1.21
150,000	1.04	1.08	1.09
200,000	1	1	1
250,000	0.93	0.93	0.93
300,000	0.88	0.88	0.87
350,000	0.83	0.84	0.83
400,000	0.79	0.80	0.79
500,000	0.72	0.73	0.82
<b>Deviation</b>	+98% to -28%	+90% to -27%	+122% to -18%

Table 15:  $C_{Re}$  values with varying Reynolds number

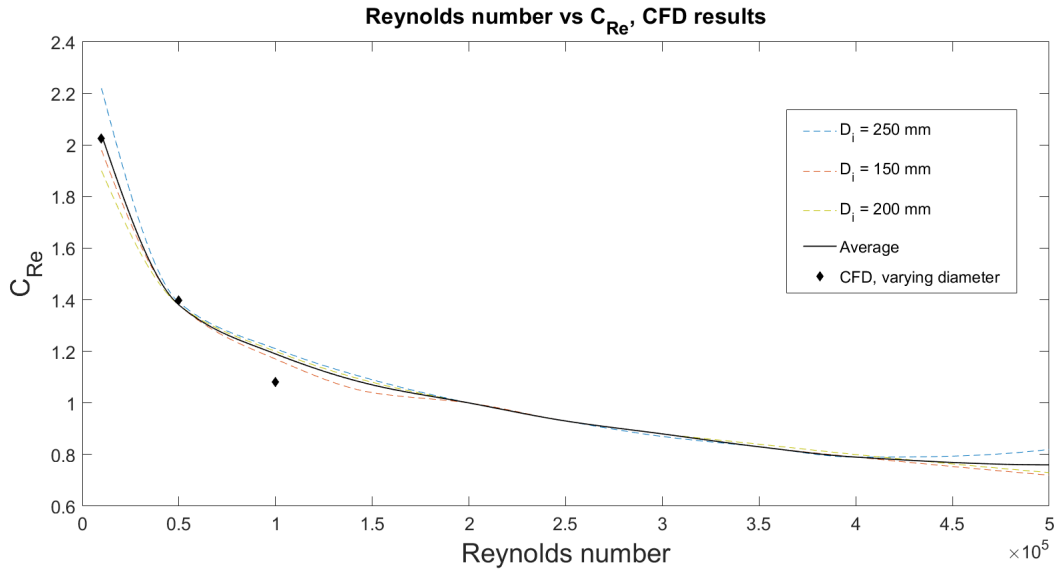


Figure 25:  $C_{Re}$  plot with varying Reynolds numbers and constant diameter

Figure 25 shows three points adapted from the varying diameter case and are obtained from figure 24. As figure 24 shows little variation in the zeta values relative to the diameter, the results were plotted as the three points in figure 25, making the predictions of the effects on Reynolds number even more solid. Based on the plot in figure 25, assumptions were made that the graph represents an exponential form, or a “power”-equation. An online regression tool was used to resolve an equation [15]. When using this tool, the equations

suggested comes with an average relative error where every point deviates from the input x- and y values. The exponential form gives an average relative error of 10.74% whereas the power equation has an average relative error of 1.75%. Therefore, a power regression on the form  $C_{Re} = aRe^{-b}$  is used from our CFD input data and led to the equation:

$$C_{Re} = 21.6(Re)^{-0.254} \quad (24)$$

The power equation is based on the average graph.

<b>Zeta values</b>			
Reynolds number	d/mm=150	d/mm=200	d/mm=250
10,000	0.547	0.505	0.574
50,000	0.38	0.365	0.358
100,000	0.323	0.318	0.311
150,000	0.286	0.288	0.281
200,000	0.276	0.265	0.258
250,000	0.257	0.248	0.24
300,000	0.241	0.234	0.226
350,000	0.229	0.222	0.213
400,000	0.218	0.212	0.203
500,000	0.199	0.195	0.211
<b>Deviation</b>	0.348	0.31	0.363

Table 16: Zeta values with varying Reynolds number

In the range of Reynolds numbers from Re=100,000 and Re=500,000 the deviations show a pattern for the three diameters, with deviations within the range of +21% to -28%, which in itself clearly states the effects of Reynolds number on pressure loss in a 90 degree smooth bend. However, when studying the range of Reynolds numbers between Re=10,000 and Re=50,000, we notice a great deviation, mainly for Re=10,000 with d/mm=250, with a relative  $\zeta$  value at 122%. We can also see an increase ranging from 38% on all other cases within this Reynolds range. Koch presented values adapted from the European Report for a smooth 90 degree bend using d=250 mm [4] and Re=200.000 as reference value:

<b>Re</b>	$C_{Re}$
50,000	1.37
100,000	1.16
150,000	1.08
200,000	1
250,000	0.99
300,000	0.98
350,000	0.97
400,000	0.96

Table 17:  $C_{Re}$  values for d/mm=250 with varying Reynolds number by Koch [4]



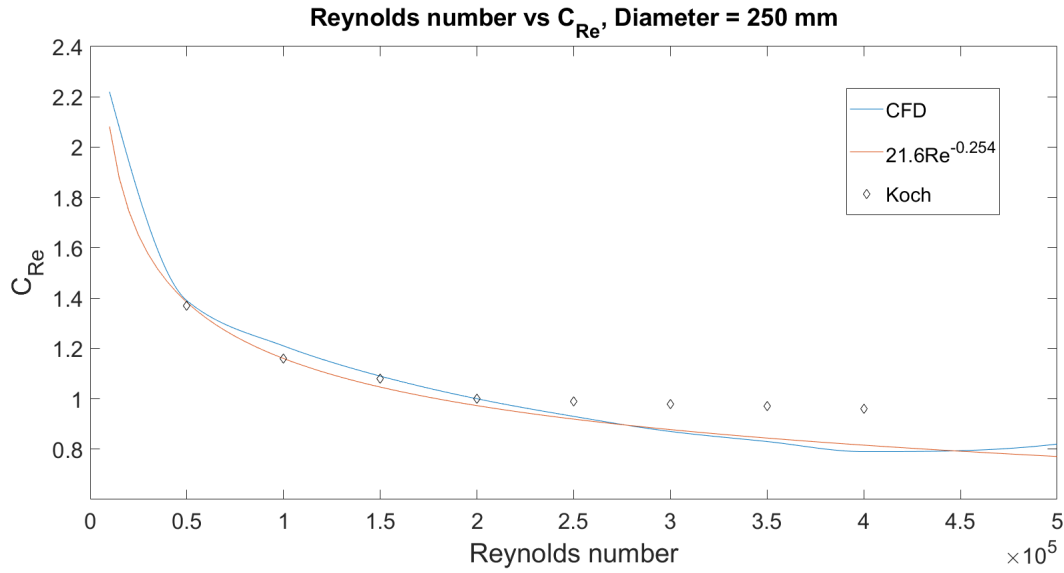


Figure 26:  $C_{Re}$  plot with varying Reynolds number and  $d/\text{mm}=250$ , comparing own results with results given by the European Report [16].

Figure 26 shows the variation of  $C_{Re}$  with  $d/\text{mm}=250$  for varied Reynolds numbers, with the reference value at  $Re=200,000$ , including our own results and results adapted from the European Report. The values presented by Koch [4] are in the range of Reynolds numbers  $50,000 \leq Re \leq 400,000$ , a slightly smaller range than our own. When observing and comparing the results, there is a similar pattern which can be interpreted as confirmation on the predictions made.

## 7 Conclusions

During our work in this thesis, including several runs not included in the report, assumptions regarding chosen properties for input data are made to help future users of STAR-CCM+ to reach their predictions. This report includes comprehensive input data accompanying all results, making the possibility for validation easier for future research. This report, however, stands out by using STAR-CCM+ as the simulation tool. Results concerning straight pipe with wall roughness and with 90 degree bends, using air as a fluid in most of the cases, are the product of several runs for different input data. All cases also have residuals converging to the value of  $10^{-6}$ . Ultimately, these results are presented with recommendations regarding turbulence models, wall treatment and mesh selections among other data.

- In the cases involving straight pipes the  $\kappa - \epsilon$  turbulence model is recommended along with the trimmer mesh.
  - When dealing with smooth pipes we recommend using  $1 < y^+ < 14$  for better accuracy.
  - For rough pipes we recommend using  $17 < y^+ < 250$ . In this range we found excellent accuracy involving error consistently below 0.7%.

Keep in mind, for all straight pipe cases, simulations are run with a prerequisite that the fluid is incompressible. In order to justify this according to the natural laws, make sure the Mach number is  $< 0.3$  for ideal gas.

- When simulating pressure loss through a circular pipe with a  $90^\circ$  bend, we recommend using the RSM turbulence model with the polyhedral mesh.

From the present study it appears that the pressure loss coefficient is not varying appreciatively with diameter. The pressure loss coefficient is a predominant function of Reynolds number for internal flows through pipes. A curve fitting shows the functional dependency as below

$$C_{Re} = 21.6(Re)^{-0.254} \tag{25}$$

for  $90^\circ$  bend in the range of  $10,000 \leq Re \leq 500,000$ . This lies within the average relative error of 1.7 % compared to results attained in this report.

## References

- [1] Sturla Ingebrigtsen. *Ventilasjonsteknikk, Del 1*. Skarland Press AS.
- [2] <https://www.thepixellab.net/air-duct-generator-for-cinema4d>. Air Duct Generator for Cinema4d.
- [3] Yunus A. Çengel and John M. Cimbala. *Fluid mechanics: fundamentals and applications*. McGraw Hill, New York, third edition edition, 2014.
- [4] P Koch. The influence of Reynolds Number and size effects on pressure loss factors of ductwork components. *Building Services Engineering Research and Technology*, 27(4):261–283, November 2006.
- [5] Mohammad Salehi, Ahmad K. Sleiti, and Stephen Idem. Study to identify computational fluid dynamics models for use in determining HVAC duct fitting loss coefficients. *Science and Technology for the Built Environment*, 23(1):181–191, January 2017.
- [6] Milovan Gutovic, Haris Lulic, and Emir Sirbubalo. *CFD Analysis of Pressure Losses in Flat-Oval Duct Fittings*. 2013.
- [7] <http://pointing.spiraxsarco.com/resources/steam-engineering-tutorials/flowmetering/fluids-and-flow.asp>. Fluid Characteristics.
- [8] H. K. Versteeg and W. Malalasekera. *An introduction to computational fluid dynamics: the finite volume method*. Pearson Education Ltd, Harlow, England ; New York, 2nd ed edition, 2007. OCLC: ocm76821177.
- [9] [https://www.cfd-online.com/Wiki/Dimensionless\\_wall\\_distance\\_\(y\\_plus\)](https://www.cfd-online.com/Wiki/Dimensionless_wall_distance_(y_plus)). Dimensionless wall distance, y plus., March 2014.
- [10] Siemens. *STAR-CCM+ Documentation, Version 12.04*, 2017.
- [11] [https://www.cfd-online.com/Wiki/Generic\\_scalar\\_transport\\_equation](https://www.cfd-online.com/Wiki/Generic_scalar_transport_equation). Generic Scalar Transport Equation.
- [12] [http://stats.cse.ucdavis.edu/InstallationGuide\\_11.04.012\\_01.html](http://stats.cse.ucdavis.edu/InstallationGuide_11.04.012_01.html). STAR-CCM+ Installation Guide.
- [13] <https://www.nuclear-power.net/nuclear-engineering/fluid-dynamics/major-head-loss-friction-loss/relative-roughness-of-pipe/>. Relative Roughness.
- [14] Bert Blocken, Ted Stathopoulos, and Jan Carmeliet. CFD simulation of the atmospheric boundary layer: wall function problems. *Atmospheric Environment*, 41(2):238–252, January 2007.
- [15] <https://planetcalc.com/5986/?license=1>. Function approximation with regression analysis, 2016.
- [16] Rue de la Loi. Energy loss coefficients of components used in air distribution systems., October 1992.

## 8 Appendix A. Residuals Straight Pipe

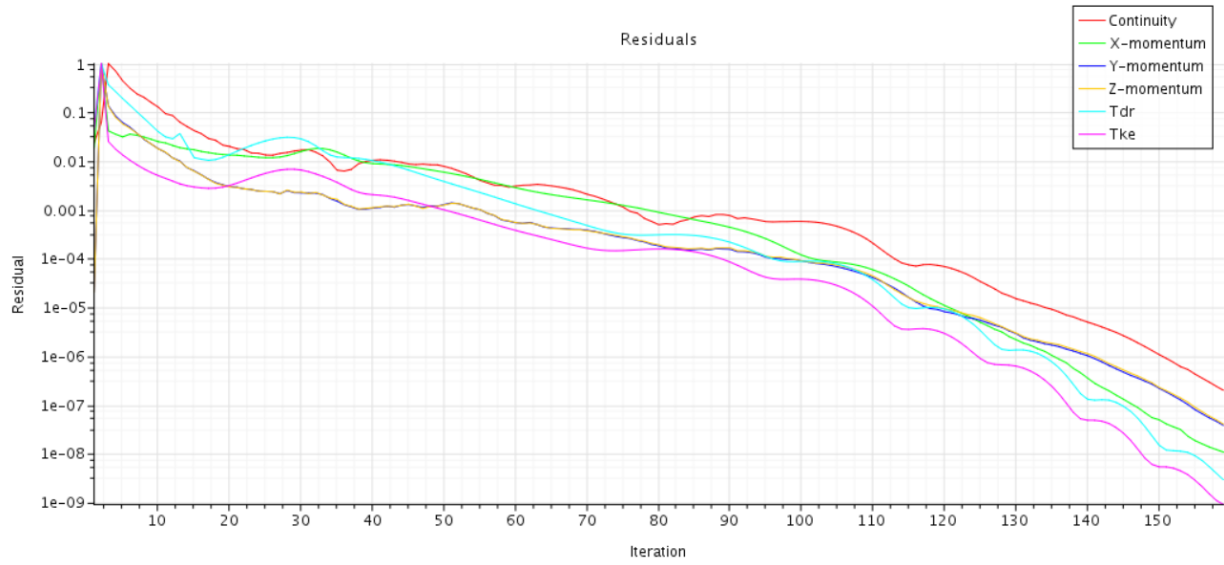


Figure 27: Residuals for Re 50,000 with  $\kappa - \epsilon$  model

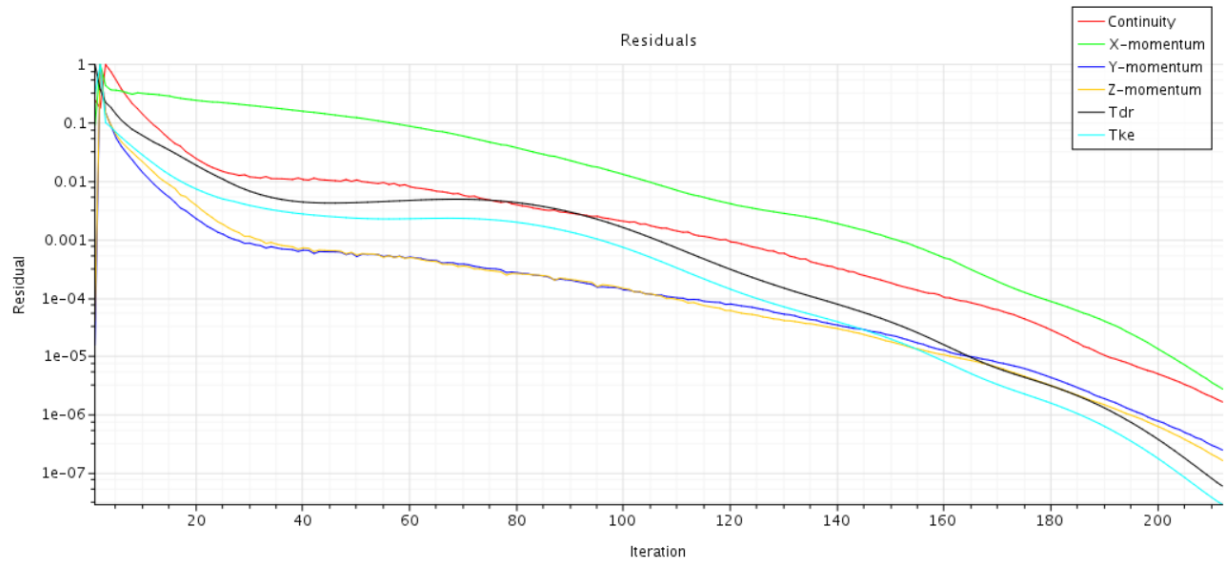


Figure 28: Residuals for Re 100,000 with  $\kappa - \epsilon$  model

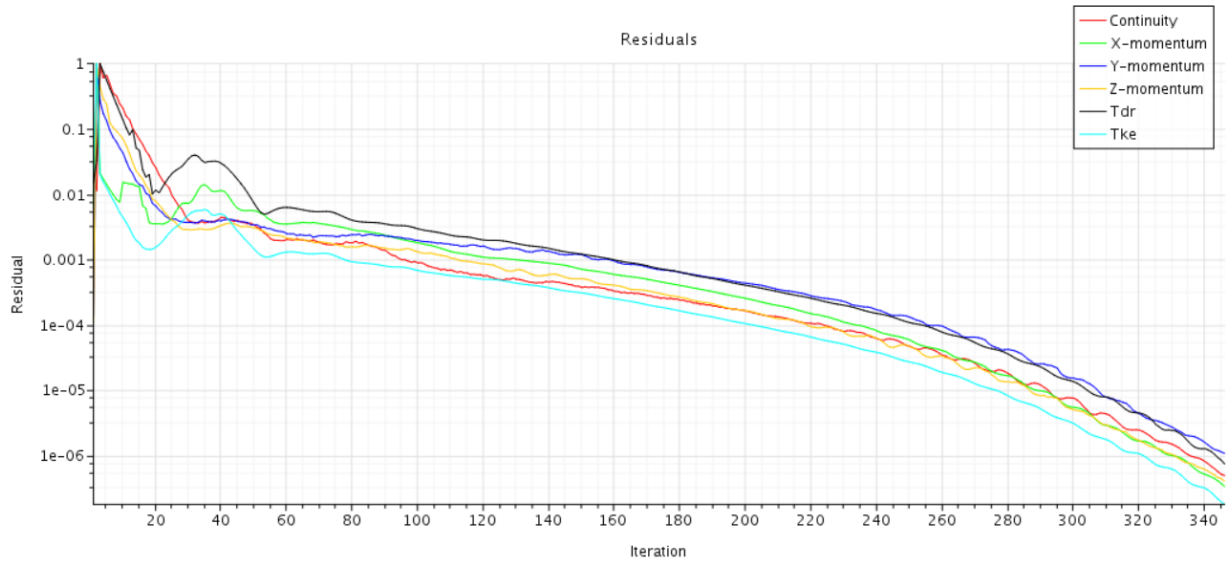


Figure 29: Residuals for Re 200,000 with  $\kappa - \epsilon$  model

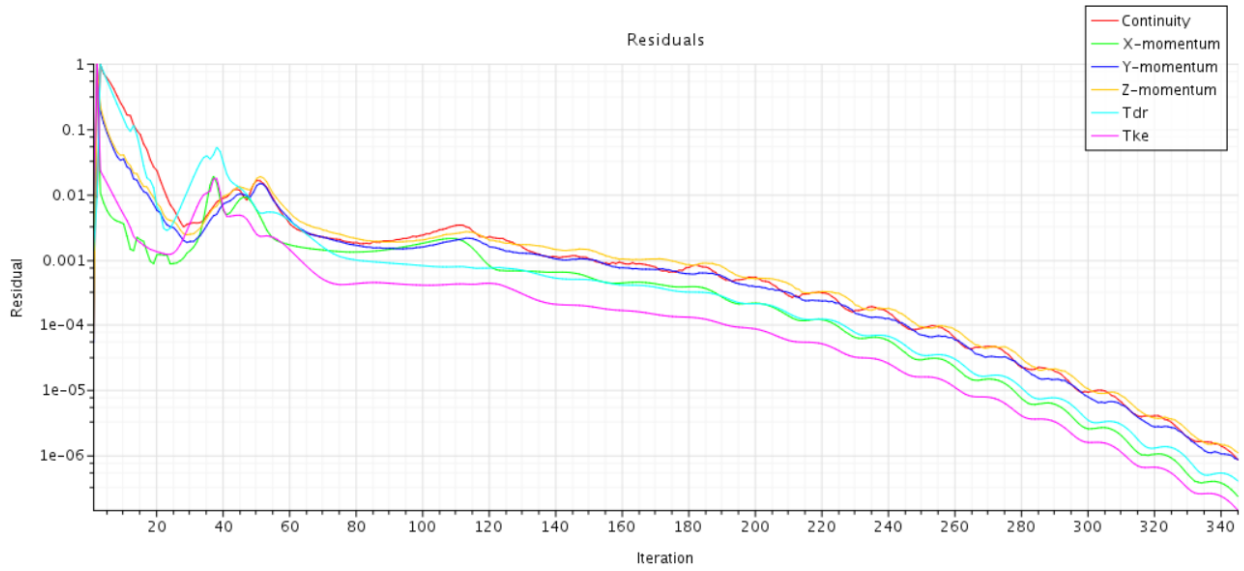


Figure 30: Residuals for Re 500,000 with  $\kappa - \epsilon$  model

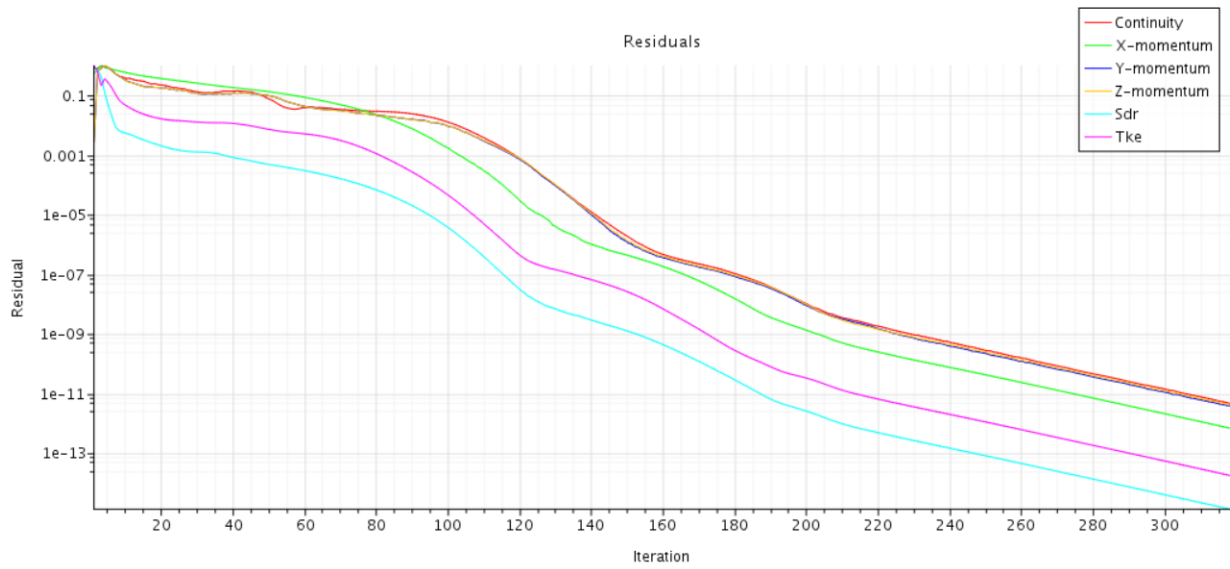


Figure 31: Residuals for Re 50,000 with  $\kappa - \omega$  model

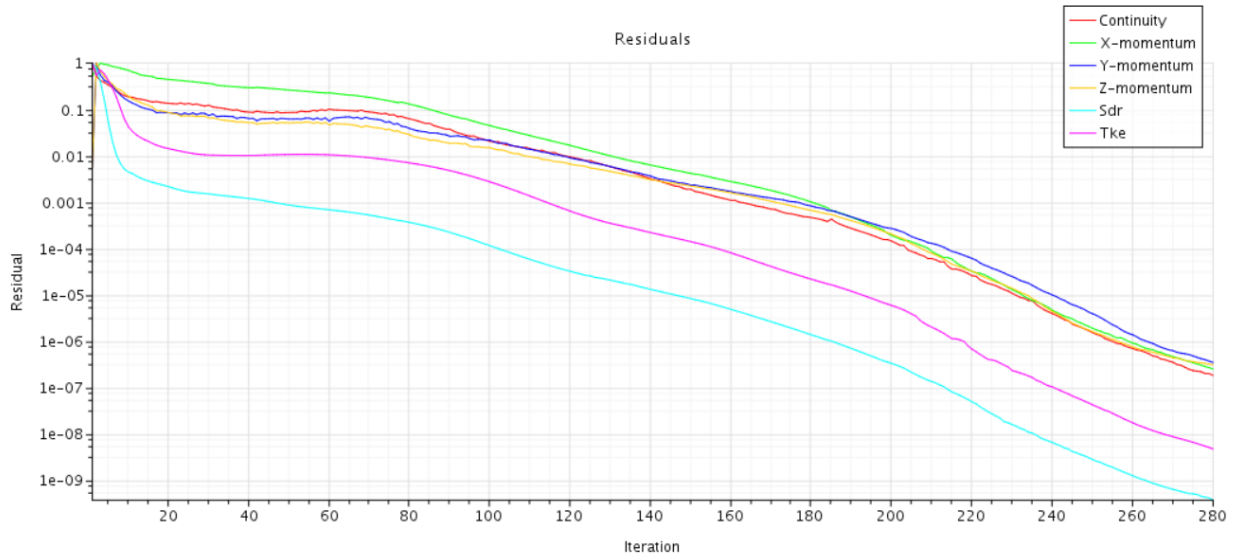


Figure 32: Residuals for Re 100,000 with  $\kappa - \omega$  model

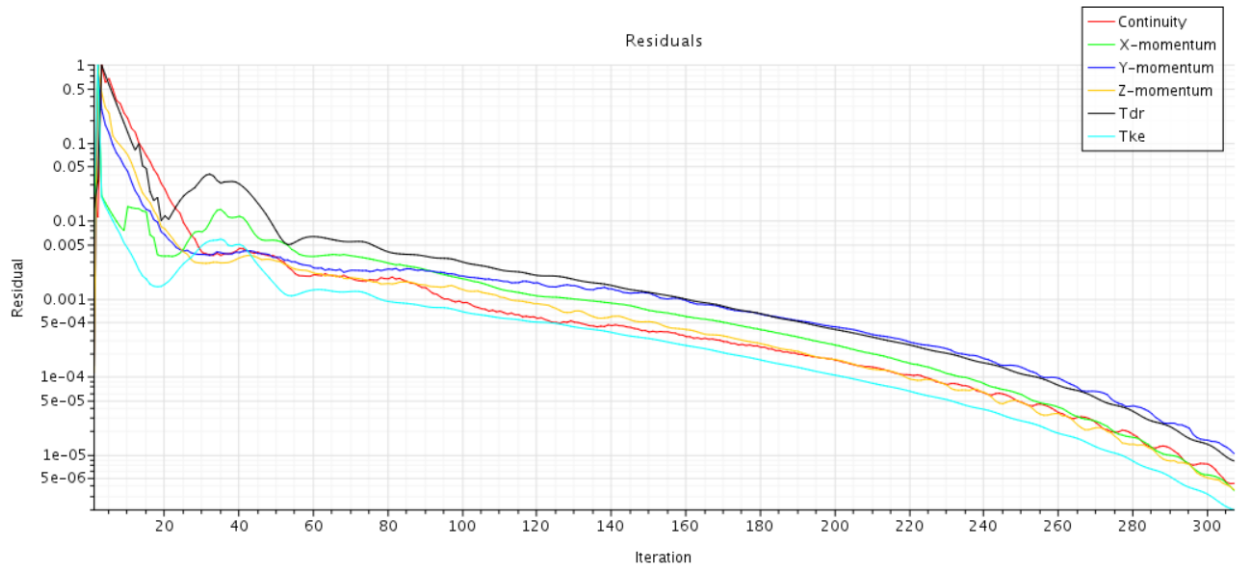


Figure 33: Residuals for Re 200,000 with  $\kappa - \omega$  model

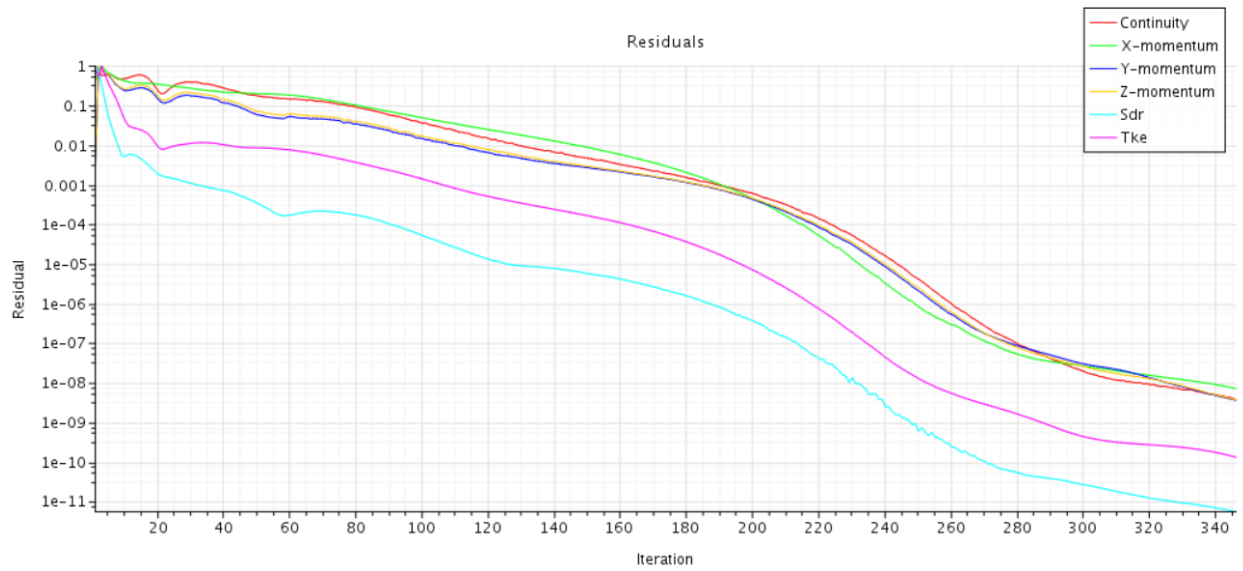


Figure 34: Residuals for Re 500,000 with  $\kappa - \omega$  model

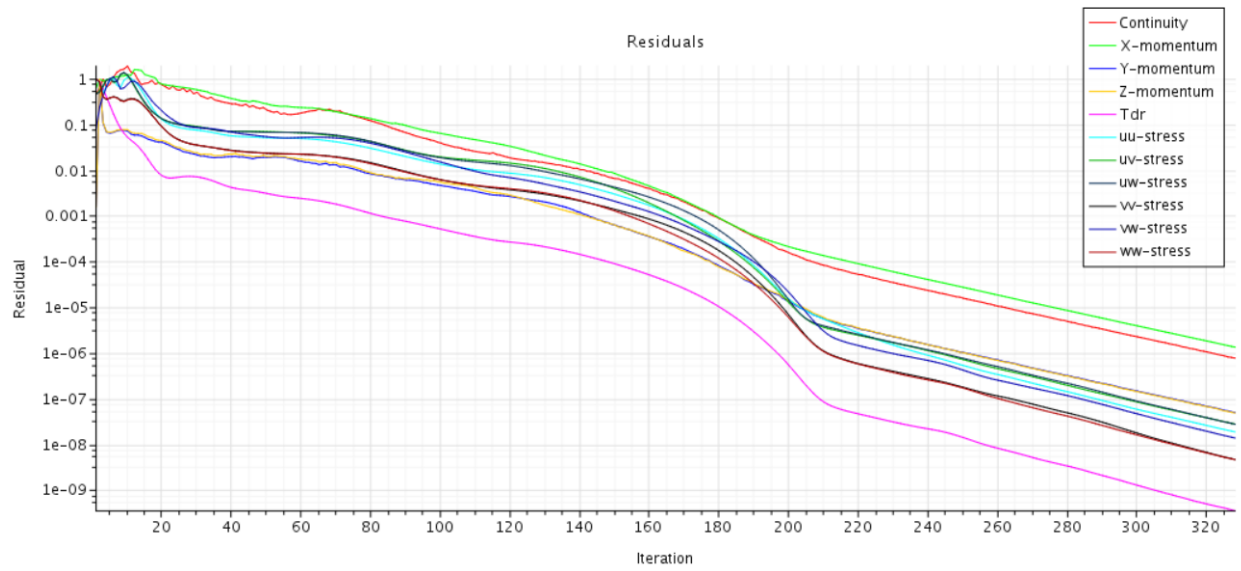


Figure 35: Residuals for Re 50,000 with RSM model

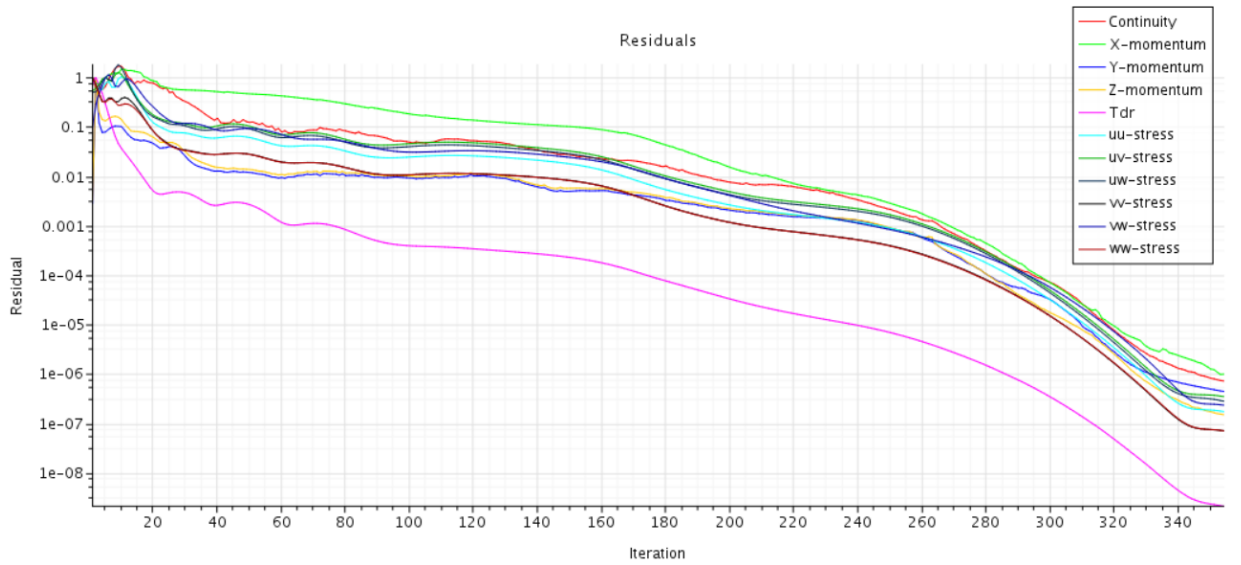


Figure 36: Residuals for Re 100,000 with RSM model



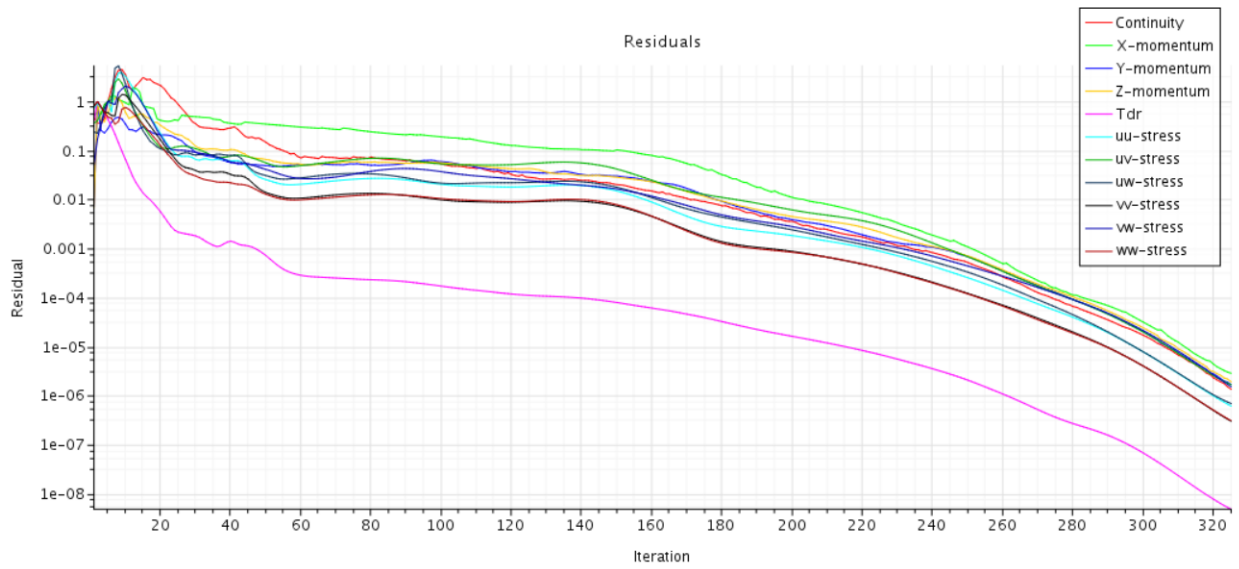


Figure 37: Residuals for Re 200,000 with RSM model

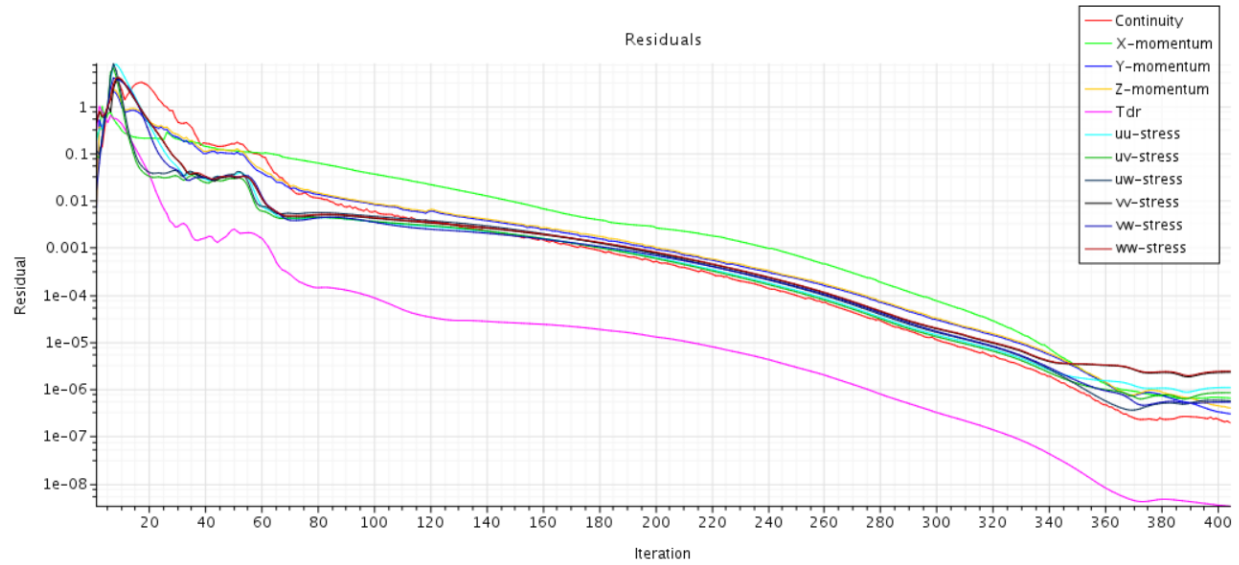


Figure 38: Residuals for Re 500,000 with RSM model

## 9 Appendix B. Residuals 90 Degree Bend

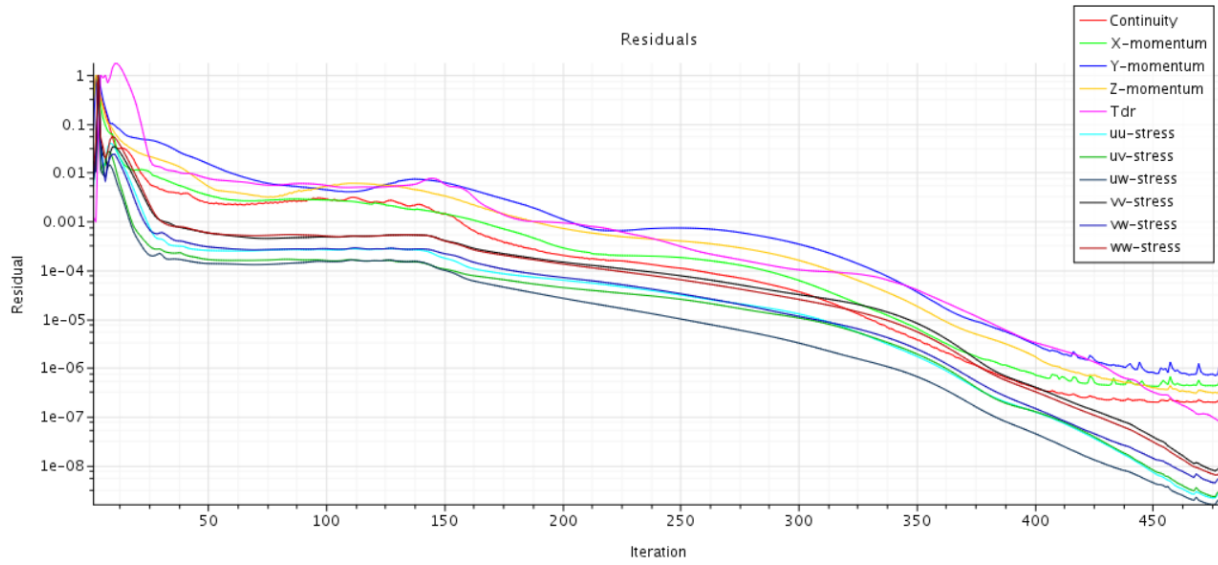


Figure 39: Residuals for Re 10,000 and  $d/\text{mm}=200$  with RSM model

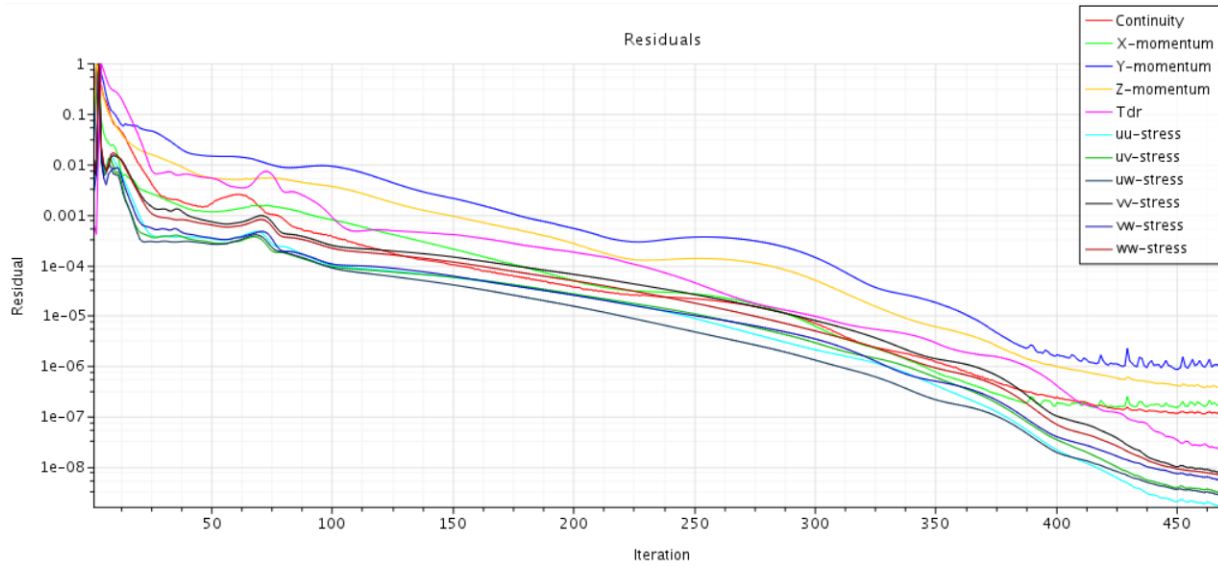


Figure 40: Residuals for Re 50,000 and  $d/\text{mm}=200$  with RSM model

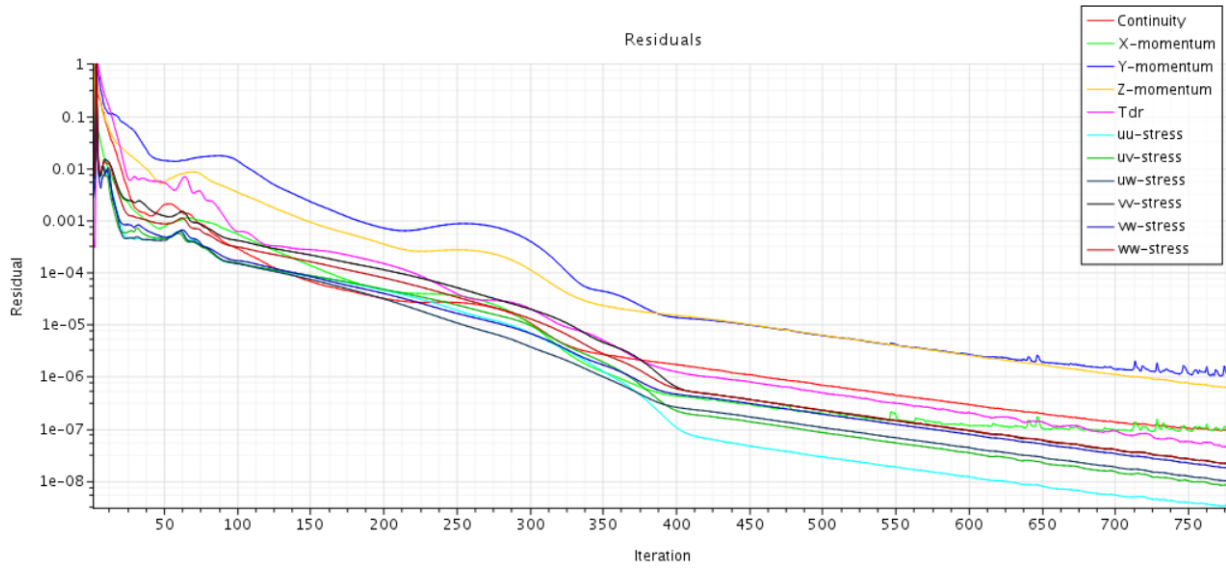


Figure 41: Residuals for Re 100,000 and d/mm=200 with RSM model

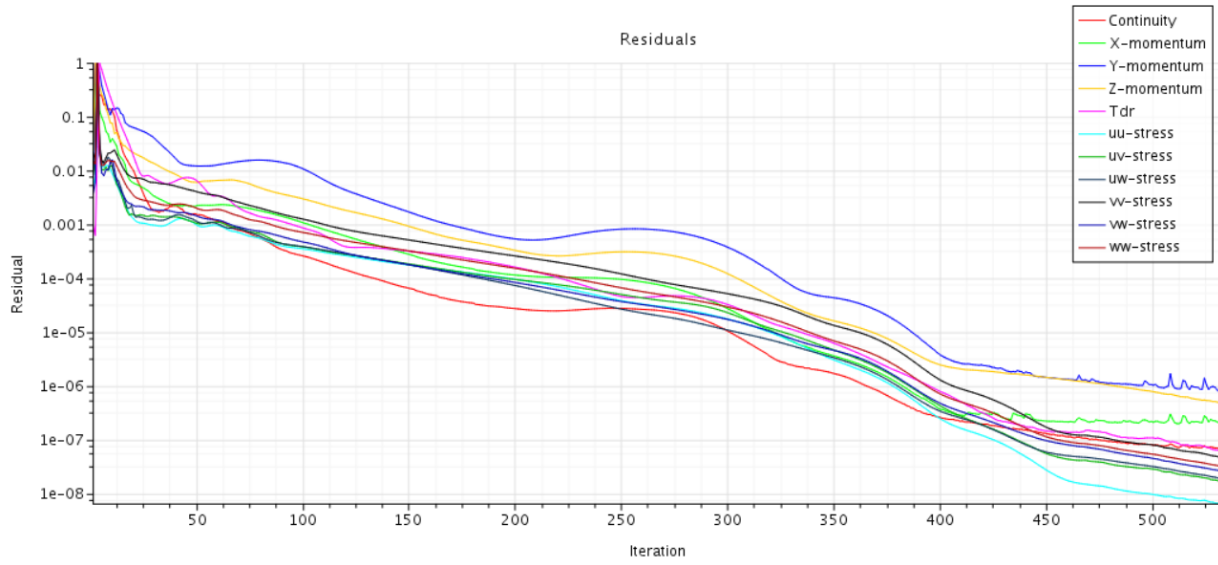


Figure 42: Residuals for Re 200,000 and d/mm=150 with RSM model

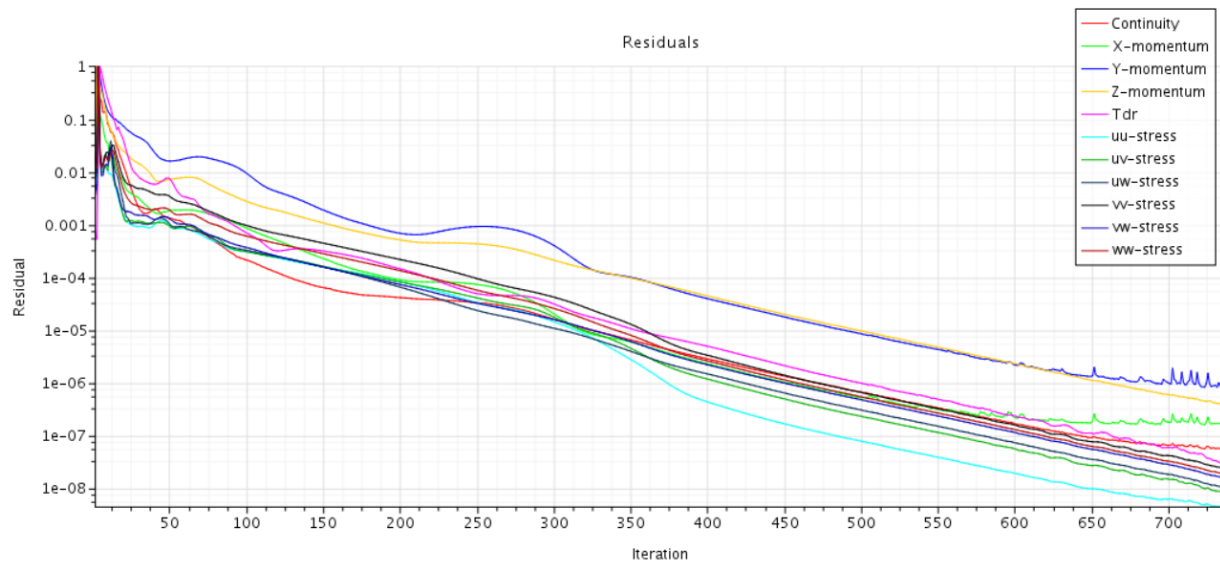


Figure 43: Residuals for Re 200,000 and d/mm=200 with RSM model

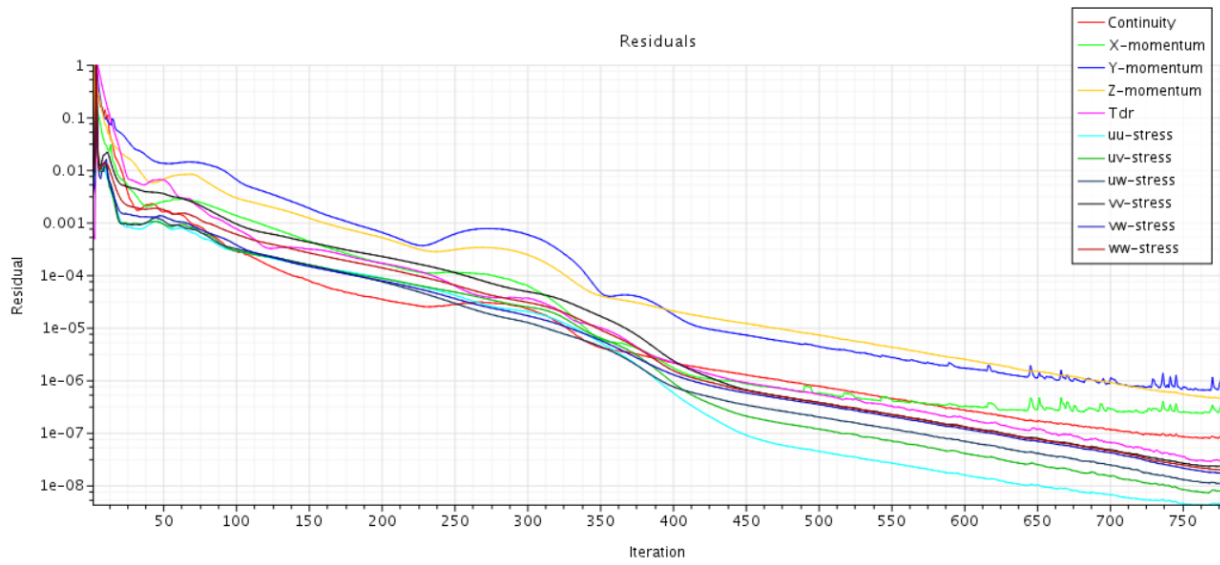


Figure 44: Residuals for Re 200,000 and d/mm=250 with RSM model